

Distributed Communication Network Wireless Siting and Propagation Studies

by

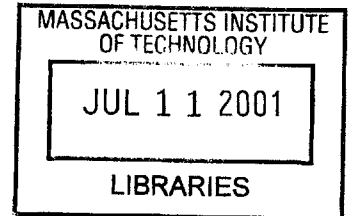
Win Chevapravatdumrong

SUBMITTED TO THE DEPARTMENT OF ELECTRICAL ENGINEERING AND
COMPUTER SCIENCE IN PARTIAL FULFILLMENT OF THE REQUIREMENTS FOR THE
DEGREE OF

MASTER OF ENGINEERING IN ELECTRICAL ENGINEERING
AT THE
MASSACHUSETTS INSTITUTE OF TECHNOLOGY

May 2001
ELECTRICAL ENGINEERING

© 2001 Win Chevapravatdumrong. All rights reserved.



BARKER

The author hereby grants to MIT permission to reproduce and to distribute publicly paper
and electronic copies of this thesis document in whole or in part and to grant others the
right to do so.

Author _____

Department of Electrical Engineering and Computer Science

Certified by _____

Michael A. Deaett
Charles Stark Draper Laboratory
Thesis Supervisor

Certified by _____

Prof. David H. Staelin
Thesis Advisor

Accepted by _____

Prof. Arthur C. Smith
Chairman, Department Committee on Graduate Theses

Distributed Communication Network Wireless Siting and Propagation Studies

by

Win Chevapravatdumrong

SUBMITTED TO THE DEPARTMENT OF ELECTRICAL ENGINEERING AND
COMPUTER SCIENCE ON MAY 18, 2001 IN PARTIAL FULFILLMENT OF THE
REQUIREMENTS FOR THE DEGREE OF

MASTER OF ENGINEERING IN ELECTRICAL ENGINEERING
AT THE
MASSACHUSETTS INSTITUTE OF TECHNOLOGY

Abstract

This thesis analyzes siting and propagation studies for a real-time unmanned aircraft navigation system and other wireless distributed control systems where the type of terrain will often be unknown. Field measurements were made of the 2.4-GHz propagation characteristics for a variety of abnormal siting situations and realistic field environments in which the systems will be deployed. The mobile test equipment consists of two small, programmable transceivers that can measure received signal strength. This equipment is programmed to facilitate automated measurements as described in the thesis. Propagation characteristics were investigated using a structured framework that divides measurements into large-scale deterministic, small-scale statistical, and large-scale statistical analysis.

Empirical data from several environments and siting situations for both large-scale and small-scale fading were collected. The large-scale deterministic measurements verified the 2-ray model and yielded a path loss exponent of $d^{2.28}$ in simple network configurations, where d is distance in meters, as well as a loss of $d^{3.87}$ in the Vvedensky region. The small-scale statistical investigations verified a close fit to Ricean-distributed multipath fading with a line-of-site path. Small-scale measurements also revealed significant changes (up to 15 dB) in propagation due to minor spatial antenna movements, as well as Doppler spread values ranging from 0.5 to 2.5 Hz. Large-scale statistical investigations determined path loss exponents for various environments over distances of up to 150 meters. These values ranged from 2.11-3.18 in urban environments to almost 4 in environments with thick vegetation.

Communication system design implications based on these results are discussed. The small-scale findings demonstrate that link level spatial redundancy is required to provide adequate network performance. The large-scale findings provide realistic distance-dependent loss data necessary for calculating network link budgets.

Faculty Thesis Supervisor: Prof. David H. Staelin

Draper Thesis Supervisor: Michael A. Deaett

Acknowledgments

I first and foremost would like to thank the Charles Stark Draper laboratory for sponsoring my research on this project. I would also like to thank my Draper advisor, Michael Deaett, for his endless technical guidance and support, as well as his help in conducting field measurements in any and all types of weather conditions. Also, I would like to thank Professor David Staelin, my MIT faculty thesis advisor, for his technical assistance and direction. Additionally, I would like to thank Robert Tingley and Vincent Attenasio from the Draper RF and Communications Group for their patience and technical help, as well as numerous other Draper employees for their support and guidance: Pat Callinan, Seth Davis, Stephen Finberg, Michael Aiken, John Ford, and Valerie Lowe. Finally, I would like to thank my family—Wichai, Suwannee, and Cherry Chevapravatdumrong—whose endless encouragement provided the motivation for the hard work that led to the completion of this project.

This page intentionally left blank

ACKNOWLEDGMENT

May 18, 2001

This thesis was prepared at The Charles Stark Draper Laboratory, Inc., under project 13046—Distributed Data Link Network Design.

Publication of this thesis does not constitute approval by Draper or the sponsoring agency of the findings or conclusions contained herein. It is published for the exchange and stimulation of ideas.

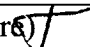
(author's signature) 

Table of Contents

1	Introduction	11
1.1	Past Work	12
1.2	Problem Description	13
1.3	Thesis Outline and Approach	13
2	Propagation Modeling Theory	15
2.1	Large-Scale Fading	17
2.1.1	Large-Scale Statistical Analysis	17
2.1.2	Large-Scale Deterministic Analysis: 2-ray Model	20
2.2	Small-Scale Fading	24
2.2.1	Distribution of Path Amplitudes	24
2.2.2	Parameters of Small-Scale Multipath Fading	26
3	Measurement System Overview	29
3.1	Commercial Hardware	30
3.2	Internal Draper Hardware: DWN Transceiver	31
3.3	DWN Transceiver Design	33
3.4	Software Design	35
3.4.1	Transmitter	35
3.4.2	Receiver	37
3.5	Packaging	40
4	Test Suite Design and Characterization	43
4.1	RSSI Characterization	44
4.2	Antenna Characterization	47
4.2.1	Antenna Resonance	48
4.2.2	Antenna Gain	48
4.3	Sampling Rate and Test Duration	50
4.4	Test Suite Summary	51
5	Large-Scale Deterministic Modeling: 2-ray Model	53
5.1	Attenuation Function Height Dependency	54
5.2	Attenuation Function Distance Dependency	57
5.3	Vvedensky Region	60
5.4	Deterministic Large-Scale Path Loss Model	61
6	Small-Scale Statistical Modeling	63
6.1	Small-Scale Amplitude Distributions	64
6.2	Coherence Time and Doppler Spread	69
6.3	Small-Scale Fading System Design Implications	72
7	Large-Scale Statistical Modeling	75
7.1	Ground-to-ground Through Vegetation	76

7.2	Urban Setting	78
7.3	Single Tree Propagation	80
7.4	Summary of Large-Scale Results	81
7.5	Large-Scale Fading System Design Implications	81
8	Conclusion	83
A	Additional Measurements	87
B	Maps and Photographs	92
C	Hardware Overview Chart	99
D	Antenna Datasheets	101
	Bibliography	107

List of Figures

2-1	Configuration for 2-ray Reflection Model	20
2-2	Method of images geometry	23
3-1	Block diagram of DWN Transceiver in transmit mode	33
3-2	Block diagram of DWN Transceiver in receive mode	34
3-3	Toko antennas	34
3-4	Receiver information flow	37
3-5	Receiver instrument setup	41
4-1	RSSI calibration curves	45
4-2	RSSI rise time	46
4-3	RSSI fall time	46
4-4	Generic field test configuration	47
4-5	Toko antenna gain characterization setup	49
5-1	2-ray height dependency measurement setup	55
5-2	Measured and theoretical values of path loss about a mean vs. receiver height .	56
5-3	General case of attenuation function	57
5-4	Briggs field calculated attenuation function vs. separation distance	59
5-5	Briggs field measured and theoretical values for path loss vs. separation distance	59
5-6	Measured values for path loss vs. separation distance in Vvedensky region . . .	61
5-7	Measured F region and Vvedensky region path loss vs. distance	62
6-1	Photographs of multipath fading measurement locations	65
6-2	Histograms of small-scale amplitude measurements	66
6-3	Path loss vs. horizontal distance for small-scale experiments	67
6-4	Time-domain and Fourier Transform Doppler spread plots	70
7-1	Path loss vs. distance at Alewife Preserve	76
7-2	Example measured values for large-scale distribution at Alewife Preserve	77
7-3	Path loss vs. distance along Vassar Street	79
A-1	Transmitter siting locations atop parking garage	88
A-2	Photographs of transmitter atop parking garage	88
A-3	Diagram of corner measurements	89
A-4	Photograph of corner measurements	90
B-1	Diagram of Alewife Preserve measurements	92
B-2	DWN transmitter 1 meter high above low-lying vegetation	93
B-3	DWN transmitter amongst low-lying vegetation	93
B-4	Diagram of measurements conducted along Vassar Street	94
B-5	Photograph of Vassar Street	95
B-6	Map of Vassar Street	95
B-7	Additional map of Vassar Street	96
B-8	Diagram of Thorndike Park measurements	97
B-9	Photograph of transmitter atop pole set in Maple tree with no foliage	98

List of Tables

3-1	DWN Transceiver specifications	32
3-2	SCI register descriptions	36
3-3	ATD register descriptions	38
4-1	Summary of Toko gains	50
4-2	Hardware and test suite summary	51
6-1	Summary of Doppler spread and coherence time measurements	71
7-1	Summary of large-scale results	81
A-1	Theoretical distribution parameters for measurements from section 6.1	91
C-1	Hardware overview	99
C-2	Hardware overview	100

This page intentionally left blank

Chapter 1

Introduction

Physical layer transmission capability is the foundation of any communication or radar system; without transmission across a given media, no information can be sent. This transmission capability for wireless systems is highly dependent upon two factors: siting and propagation. Siting refers to placing a communication device in an environment so that it can radiate from its immediate surroundings. Having sited two devices, propagation refers to the ability to transmit energy directly from one device to the other in that given environment.

The purpose of this project is to perform siting and propagation studies for a real-time unmanned aircraft navigation system and other distributed control systems employing wireless connectivity. The navigation system acts as a wireless network with Grid Relay Stations (GRS units) that transmit updated location and destination coordinates to in-flight aerial users. The system is designed as a pre-planned network, meaning it is deployed according to an infrastructure plan developed before system utilization. The

results of this project's studies are useful in the performance prediction phase of network planning.

One important feature that differentiates the navigation system from other wireless navigation systems is its method of deployment. The GRS units are arranged or simply dropped in the local area between the source and destination sites. While such an ad-hoc network offers flexibility in topology and host distribution, it should be noted that the type of terrain in which the system is deployed will often be unknown. For this reason, it is necessary to conduct propagation studies in different environments and topologies in order to simulate possible deployment configurations.

1.1 Past Work

Extensive work has been performed in the realm of propagation modeling. Demand for such studies is due mostly to the worldwide rollout of cellular mobile communication systems and wireless LANs. Indoor radio propagation modeling work can be found in [1-4]. Outdoor studies for cellular systems have also been performed [5-10]. These studies are all helpful in understanding various methods and waveforms used for propagation modeling. Such work is often based on commonly used mathematical and statistical models. Some of these models include the Longley-Rice, Hata, and Okumura models [11-13].

Since most published propagation work has been tailored specifically for cellular applications, findings are not applicable to the navigation system. In cellular applications and models, larger communication distances and tall base stations are assumed. For example, the Longley-Rice model does not apply for distances < 1 km. There only exist

a few studies that explore the type of configurations required by the navigation system [14-15].

1.2 Problem Description

As such, there is clearly a need for further studies more specific to the requirements of the navigation system. This project will focus on two primary issues of concern: propagation characteristics of radio frequency (RF) waves through a variety of environments, as well as siting methods for the distributed wireless components (GRS units) of the system. Measurement hardware must be developed that is capable not only of performing the necessary tests, but also of enabling mobility of the test equipment.

1.3 Thesis Outline and Approach

Chapter 2 begins with explanations of the manner in which propagation modeling was performed. A framework is introduced around which the measurements were based. An overview of theory for both large-scale and small-scale modeling is offered, as well as a discussion detailing the difference between deterministic and statistical modeling. Equations are developed that serve as foundations for the propagation measurements.

Next, Chapter 3 is an overview of the hardware selection process and reasons for why the DWN transceiver was selected as the measurement system. Discussion then moves to the topic of the transceiver itself—how it is designed, how it functions, etc. Design of the entire measurement system will then be reviewed, including software design, hardware fixes, and equipment packaging.

Chapter 4 is an explanation of how the propagation measurements were actually performed. It reviews how the hardware was characterized, as well as how results of the measurement system can be used for propagation modeling. A test suite summary is discussed, detailing the manner in which each measurement is made.

Chapter 5 is the first chapter presenting results from propagation measurements. It discusses data gathered from large-scale deterministic experiments and formulates a model for low-ground communication in open environments. More theory about the 2-ray model beyond what is discussed in Chapter 2 is presented.

Chapters 6 and 7 contain the more comprehensive statistical propagation studies. Small-scale measurements are discussed in Chapter 6 and results are analyzed. Chapter 7 offers similar content, but overviews the large-scale measurements.

Finally, Chapter 8 summarizes the project and discusses the importance of the work towards what is needed by the navigation system for network design. Possibilities for future work are also suggested.

Chapter 2

Propagation Modeling Theory

There are many complex mechanisms that govern radio propagation, and in a wireless ad-hoc communication system, these mechanisms vary vastly across different environments. Mechanisms that govern radio wave propagation are often separated into three different contributing phenomena: reflection, diffraction and scattering [11].

- *Reflection.* Reflection occurs when a radio wave bounces off of a flat surface whose dimensions are much larger than the wavelength of the propagating wave.
- *Diffraction.* Diffraction occurs when there is a large impenetrable body between transmitter and receiver. Secondary waves essentially “bend” behind the object, causing signal reception at the receiver even without line-of-sight (LOS).
- *Scattering.* Scattering is due to the existence of objects small compared to the wavelength of the propagating wave. Energy is re-radiated by these objects, causing the signal to “scatter” in various directions.

When these three phenomena work in conjunction to alter a signal, numerous paths of different strengths, phases, and arrival times may arise, making a received signal very unpredictable.

Propagation modeling measurements seek to provide either a deterministic analysis of these mechanisms or a statistical model detailing on average how these mechanisms will behave. Deterministic analysis involves using physics and simple analysis of radio wave propagation to accurately predict and explain the results of field measurements. Statistical modeling is in essence a reverse process, where statistics of channel parameters are derived based on these measurements.

This project seeks to mitigate the unpredictability of radio wave propagation in wireless ad-hoc communication systems by using a framework containing both deterministic analysis as well as statistical modeling. The framework is built around the idea that propagation characteristics of wireless channels can be analyzed using two different classes of fading effects: large-scale and small-scale.

Large-scale fading refers to average signal power attenuation or path loss due to distance variations. It also refers to attenuation variations exhibited when a channel's physical structure changes significantly for local areas with the same antenna separation but different transmitter/receiver geometry. Large-scale fading is generally affected by reflection or diffraction off of large objects [19]. Small-scale fading refers to signal strength fluctuations over a short period of time or distance due to multiple scatterers.

Generally in most outdoor environments, a received signal is affected by a combination of the two phenomena. This signal is often modeled as a small-scale component superimposed upon the slow variations seen in large-scale fading.

Understanding both phenomena—and being able to separate their contributions to overall signal fluctuation—is important to the design specifications of radio communication systems.

2.1 Large-Scale Fading

Large-scale fading can be examined from the perspective of either deterministic analysis or statistical modeling. The application of one or the other approach is dependent upon a given outdoor setting. In a complex setting with numerous obstructions, a signal will experience unpredictable phase and amplitude fluctuations. Because of the difficulty in deterministically quantifying such alterations to the signal, a more realistic approach to modeling these situations is to perform statistical analysis based on field measurements. In settings with minimal obstructions, radio wave propagation can be reduced to simple models based on reflection. In such cases, a physics-based deterministic approach is used [16]. This project will investigate large-scale fading phenomenon using both techniques.

2.1.1 Large-Scale Statistical Analysis

In large-scale studies, one purpose of field measurements is to provide a way of calculating path loss as a function of distance. Such information is essential in determining the size of the coverage area for a radio communication system in any environment, as well as understanding optimum antenna deployment locations [4]. This path loss can be expressed as attenuation of received power in terms of transmitted power. Ideal radio wave propagation assumes that a signal is sent between transmitter and receiver through free space. However, the three aforementioned mechanisms

contribute significantly to path loss, and therefore free space is an inaccurate representation of the propagation that actually occurs. Statistics of path parameters must be determined in order to estimate the performance of a signal across any non-ideal wireless channel exhibiting such behavior.

Large-scale fading statistics with respect to this path loss refer to calculating a mean path loss, as well as a variation about this mean [17]. Path loss can also be viewed in terms of an n th-power law—the mean received signal power fades exponentially (to the n th power) as a function of distance from a transmitter [18].

The large-scale statistical analysis and measurements to be made will be based on the path-loss exponent model. In order to clearly understand how and why this model describes a wireless channel, it is important to view its derivation based on the physics of radio wave propagation.

The Friis equation is a simplified model of radio wave propagation in a single-path free space channel. It expresses the level of received power P_r in terms of transmitted power P_t . In free space, this relationship is given by:

$$\frac{P_r}{P_t} = G_t G_r \left(\frac{\lambda}{4\pi d} \right)^2 \quad (2.1)$$

where G_t and G_r are the respective gains of the transmitter and receiver antennas, λ is the signal wavelength, and d is the antenna separation distance. If we define

$P_1 = P_t G_t G_r \left(\lambda / 4\pi d_0 \right)^2$ as the received power at a reference distance d_0 , then we can reduce Equation 2.1 to:

$$P_r = \frac{P_1 d_0^2}{d^2} \quad (2.2)$$

As previously mentioned, path loss can be viewed in terms of an n th power law where received signal power fades exponentially (to the n th power) as a function of distance from a transmitter. In free-space, the value of n —the path-loss exponent or distance-power gradient—is 2. However, in non-ideal environments, this value usually ranges anywhere from 2 to 6. Therefore, extending Equation 2.2 to a non-ideal environment where obstructions are present, the received signal power P_r can be expressed as a function of distance d between transmitter and receiver:

$$P_r = \frac{P_1 d_0^n}{d^n} \quad (2.3)$$

This distance-power relationship can be also expressed in decibels (dB) as:

$$10 \log_{10} P_r = 10 \log_{10} P_1 - 10n \log_{10} (d / d_0) \quad (2.4)$$

If we define the path loss in decibels at a distance of d_0 as $L_0 = 10 \log_{10} P_1 - 10 \log_{10} P_0$ [16], the path loss L_p in dB for an environment with a loss exponent n can be expressed as:

$$L_p = L_0 + 10n \log_{10} (d / d_0) \quad (2.5)$$

Equation 2.5 is the definition of path-loss found in [11, 16-18].

This distance-power relationship only represents a mean value, though, and in order to create an adequate large-scale path loss model for an arbitrary wireless channel, it is necessary to provide for statistical variations about this mean due to changes in the environment. This variation is often modeled in [17] as a random variable with a log-normal distribution (see section 7.1). Taking this into consideration, we arrive at the path-loss exponent model:

$$L_p = L_0 + 10n \log_{10} (d / d_0) + X_\sigma \quad (2.6)$$

where X_σ is a zero-mean Gaussian random variable with standard deviation σ .

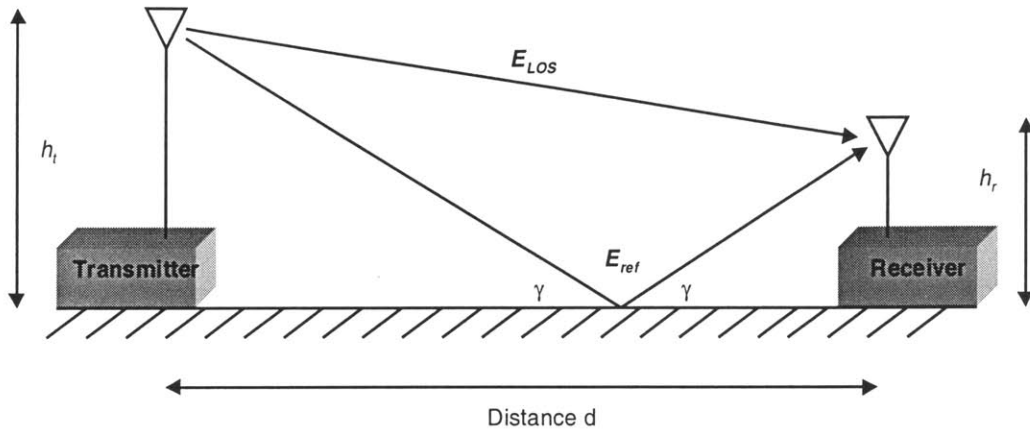


Figure 2-1: Configuration for 2-ray reflection model.

2.1.2 Large-Scale Deterministic Analysis: 2-ray Model

In simpler network configurations where obstructions between transmitter and receiver are limited, it is possible to use a deterministic physics-based approach to propagation modeling. Figure 2-1 shows the necessary configuration in which such an approach applies. It is clear that radio transmission in a simplified configuration can be treated as the sum of a line-of-sight ray and a ground-reflected ray. The appearance of this second ray alters the E-field at the receiver, and thus the Friis free-space propagation given in Equation 2.1 is inaccurate. Dolukhanov [19] redefines propagation taking into account this reflected ray and includes in his model an attenuation function F where free-space propagation loss can now be defined as:

$$\frac{P_r}{P_t} = G_t G_r \left(\frac{\lambda F}{4\pi d} \right)^2 \quad (2.7)$$

F in Equation 2.7 is dependent upon the geometry of the network configuration, as well as the surface off of which the radio wave is reflected.

The free-space rms and peak strengths of an E-field in mV/m at a receiver are given in [19] by:

$$E_{rms} = 173 \frac{\sqrt{P_1 G_1}}{d} \quad (2.8)$$

$$E_{peak} = 245 \frac{\sqrt{P_1 G_1}}{d} \quad (2.9)$$

where P_1 is the output power of a transmitter in kW, G_1 is the transmitter antenna gain, and d is the distance between transmitter and receiver in km. Accounting for the attenuation function F , Dolukhanov defines the altered E-field as:

$$E_{rms,F} = 173 \frac{\sqrt{P_1 G_1}}{d} F \quad (2.10)$$

From 2.1.1, reflection occurs when a radio wave bounces off of a flat surface whose dimensions are much larger than the wavelength of the propagating wave. Reflection of a radio wave from an imperfect conductor (i.e. the earth's surface) changes both the amplitude and phase of the wave. This change can be described in terms of a complex reflection coefficient $\mathbf{R} = R e^{-i\theta}$ where R yields the change in amplitude and θ the change in phase. To find the values of R and θ for a surface, [19-21] can be used. First, the dielectric constant ϵ and conductivity σ of the surface must be known. These values for various surfaces can be found in Chapter 2 of [19]. Using these values, charts from [20-21] can be used to estimate R and θ .

Based on radio wave reflection theory, the peak E-fields in mV/m for the LOS and reflected rays in Figure 2-1 are given by:

$$E_{LOS} = 245 \frac{\sqrt{P_1 G_1}}{d} e^{i\alpha} \quad (2.11)$$

$$E_{ref} = R \bullet 245 \frac{\sqrt{P_1 G_1}}{d + \Delta d} e^{i(\omega t - \theta - \frac{2\pi}{\lambda} \Delta d)} \quad (2.12)$$

where ω is the phase in radians of the original ray and R and θ are the amplitude and phase of the complex reflection coefficient of the reflector. Δd is the difference in path length between the LOS ray and the reflected ray. Since $\Delta d \ll d$ in all practical cases, the total peak E-field at the receiver in Figure 2-1 is defined by Dolukhanov in [19] as:

$$E_{total} = E_{LOS} + E_{ref} = 245 \frac{\sqrt{P_1 G_1}}{d} [1 + \text{Re}^{-i\beta}] e^{i\omega t} \quad (2.13)$$

where $\beta = \theta + (2\pi/\lambda)\Delta d$. Further mathematical manipulation yields the rms value of the received field:

$$E_{total,rms} = 173 \frac{\sqrt{P_1 G_1}}{d} \sqrt{1 + 2R \cos(\theta + \frac{2\pi}{\lambda} \Delta d) + R^2} \quad (2.14)$$

Comparing Equation 2.14 with Dolukhanov's equation for the altered received E_{rms} field, it is clear that the attenuation function F can be defined as:

$$F = \sqrt{1 + 2R \cos(\theta + \frac{2\pi}{\lambda} \Delta d) + R^2} \quad (2.15)$$

The *method of images* [11] in Figure 2-2 can be used to find the value of the path-length difference Δd in Equation 2.15. The lengths of the LOS ray d_{LOS} and the reflected ray d_{ref} in meters are:

$$d_{LOS} = \sqrt{(h_t - h_r)^2 + d^2} \cong d + \frac{h_t^2 - 2h_t h_r + h_r^2}{2d} \quad (2.16)$$

$$d_{ref} = \sqrt{(h_t + h_r)^2 + d^2} \cong d + \frac{h_t^2 + 2h_t h_r + h_r^2}{2d} \quad (2.17)$$

where h_t and h_r are the transmitter and receiver heights in meters and d is the antenna separation distance in meters.

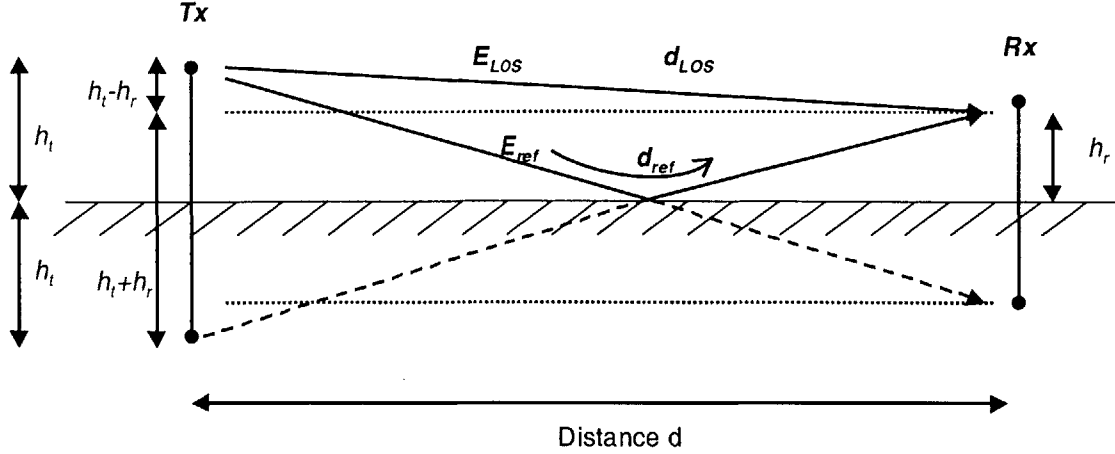


Figure 2-2: Method of images geometry.

Since Δd is simply defined as $d_{ref} - d_{LOS}$, subtracting Equation 2.16 from 2.17 gives (in meters):

$$\Delta d = d_{ref} - d_{LOS} \cong \frac{2h_t h_r}{d} \quad (2.18)$$

As such, the attenuation function F can be redefined as:

$$F = \sqrt{1 + 2R \cos\left(\theta + \frac{4\pi h_t h_r}{\lambda d}\right) + R^2} \quad (2.19)$$

Assuming perfect ground reflection ($R=1$) and a small grazing angle ($\theta=180^\circ$), Equation 2.19 can be simplified even further:

$$F = 2 \left| \sin \frac{\pi}{\lambda} \Delta d \right| = 2 \left| \sin \frac{2\pi h_t h_r}{\lambda d} \right| \quad (2.20)$$

Under these perfect assumptions, Dolukhanov [19] states that the received E-field can then be defined as the free-space E-field multiplied by F in Equation 2.20. This definition is also found in the classic 2-ray model derived by Rappaport in [11].

2.2 Small-Scale Fading

Unlike its large-scale counterpart, small-scale fading is not dependent so much on reflection and diffraction as it is on the mechanism of scattering. Scattering causes an effect of having two or more versions of the transmitter signal arrive at the receiver at slightly different times. This phenomenon, called multipath fading, can lead to a received signal that varies widely in amplitude and phase with small changes in time or travel distance [11].

2.2.1 Distribution of Path Amplitudes

Understanding received signal strength fluctuations across small travel distances or time intervals is crucial in small-scale fading analysis. The transmit power of an ad-hoc communication system can be designed to accommodate such fading. In a multipath environment, numerous distributions have been used to describe the small-scale fading envelope. The type of distribution often depends on environment, as well as the absence or presence of a dominating LOS component [4].

Rayleigh Distribution

Clarke [23] first used the Rayleigh distribution to model a mobile channel multipath fading envelope in absence of a strong line-of-sight component. The probability density function of the distribution is given by:

$$\Pr(r) = \frac{r}{\sigma^2} \exp\left\{-\frac{r^2}{2\sigma^2}\right\}, \quad r \geq 0 \quad (2.21)$$

where the mean, variance, and median are defined as $\sigma\sqrt{\pi/2}$, $\sigma^2(2 - \pi/2)$, and 1.177σ , respectively. Theoretical explanations of the applicability of the Rayleigh distribution to multipath environments can be found in [4] and [22].

Ricean Distribution

The Ricean distribution is said to occur when a strong LOS or dominant signal component exists between transmitter and receiver. The received signal then consists of the multipath Rayleigh vector, as well as a vector deterministic in amplitude and phase, representing the LOS path. The pdf of the distribution is given by:

$$\Pr(r) = \frac{r}{\sigma^2} \exp\left\{-\frac{r^2 + \nu^2}{2\sigma^2}\right\} I_0\left(\frac{r\nu}{\sigma^2}\right) \quad (2.22)$$

where I_0 is the zeroth-order modified Bessel function of the first kind, ν is the magnitude of the dominant component, and σ^2 is the variance of the multipath. The Ricean distribution is often described in terms of the Ricean factor K , defined as $K = \nu^2/2\sigma^2$. Further discussion of the theoretical relationship between this distribution and LOS multipath fading can be found in [4] and [11].

Log-normal Distribution

This distribution, as discussed in Section 2.1.1, is often used to describe large-scale variations of signal amplitudes in a given environment. The pdf is given by:

$$\Pr(r) = \frac{1}{\sigma r \sqrt{2\pi}} \exp\left\{-\frac{(\ln r - \mu)^2}{2\sigma^2}\right\} \quad (2.23)$$

In this distribution, $\log r$ is normally distributed with mean μ and standard deviation σ . Theoretical explanations for this distribution in large-scale fading can be found in [4] and [23].

2.2.2 Parameters of Small-Scale Multipath Fading

The scattering of small-scale fading is caused by two mechanisms [11, 17]:

- 1) Time-dispersion resulting from the characteristics of the fading channel's impulse response.
- 2) Time-variance resulting from slight antenna movement or spatial changes in the local environment

Bello [24] first introduced a way to model such fading phenomenon by treating the mobile channel as exhibiting wide-sense stationary uncorrelated scattering (WSSUS). More specifically, the WSSUS channel is wide-sense stationary in both time and frequency domains and also exhibits uncorrelated multipath scattering at the receiver [24]. This model can be used to describe the time-dispersive and time-variant nature of the multipath channel [11, 17, 24].

Time Dispersion: Delay Spread and Coherence Bandwidth

The multipath intensity profile is a function defined by Bello [24] that plots a channel's received power impulse response versus time delay τ [17] in seconds. The maximum excess delay is defined as the time delay during which multipath signal power falls a certain threshold below the maximum value [11, 17]. A mean excess delay and rms delay spread can also be calculated from the multipath intensity profile, where the mean

excess delay $\bar{\tau}$ is the first moment and rms delay spread σ_τ is the square-root of the second central moment of the multipath intensity profile [4].

Coherence bandwidth B_c (Hz) is a statistical measure of the frequency bandwidth over which the channel passes all spectral components with approximately equal gain and linear phase [11, 17]. Several different sources define B_c in terms of rms delay spread, though these sources vary in the exact mathematical relationship between the two parameters [17]. In [11], B_c is defined as the bandwidth where the frequency correlation function exceeds 0.5, so $B_c \approx 1/5\sigma_\tau$.

Time-Variance: Coherence Time and Doppler Spread

Time-variance in a channel is caused by slight motion of or between the transmitter and receiver in the ad-hoc communication system. It is well known that such motion causes the received frequency to be shifted relative to the transmitted frequency. This shifting, the Doppler frequency shift, f_d , is given as [16]:

$$f_d = \frac{v_m}{c} f_c \quad (2.24)$$

where v_m is the speed of motion of or between transmitter and receiver and f_c is the transmitted frequency. Doppler spread B_D (Hz) is defined in [11, 16] as being twice the Doppler shift, or the bandwidth from $f_c - f_d$ to $f_c + f_d$ in the Doppler power spectrum $D(\lambda)$, a plot of magnitude versus frequency that represents the strength of shifts at different frequencies. A more specific measure of Doppler spread, the rms Doppler spread (Hz), is defined in [25] as:

$$B_{D-rms} = \left[\frac{\int_{-\infty}^{\infty} \lambda^2 D(\lambda) d\lambda}{\int_{-\infty}^{\infty} D(\lambda) d\lambda} \right]^{\frac{1}{2}} \quad (2.25)$$

Coherence time T_C (seconds) is a statistical measure of the time duration over which the channel impulse response is invariant [11]. The approximate relationship between Doppler spread and coherence time is given by [11, 17]:

$$T_C \approx \frac{1}{B_{D-rms}} \quad (2.26)$$

This chapter developed a framework around which to perform propagation measurements based upon large-scale and small-scale fading theory. Based on this framework, experiments were designed for the field measurements. The next step was to build hardware and equipment to perform these measurements.

Chapter 3

Measurement System Overview

While many past propagation modeling efforts have been performed using large, immobile equipment such as network analyzers, the emphasis on this study was to provide not only capable measurement hardware, but also equipment that would mimic the siting methods of mobile networks. Therefore, while investigating hardware options for the study, two primary questions were raised:

- 1) What is the measurement capability of the hardware?
- 2) What is the siting flexibility of this unit?

Previous discussions have reviewed the two different types of fading classes to be studied: large-scale and small-scale. Knowledge of both phenomena is critical when designing a communication system to function across a wireless channel. The former question addresses this need. In designing the propagation modeling hardware, finding equipment with the capability to perform such measurements was essential. The latter question involves examining the size of the hardware and how the hardware can be packaged. For the studies to mimic various siting methods, ideal measurement

equipment should consist of both a mobile transmitter and receiver, i.e. no large analyzers. The hardware can then be deployed into any abnormal network configuration.

3.1 Commercial Hardware

While the emphasis on this study was to perform propagation modeling experiments, a secondary effort was dedicated to developing or altering hardware for these measurements. Additionally, upgrade capability of the hardware to a data communication network was considered. As such, initial hardware investigations focused on examining readily available commercial products with network communication capability (see Appendix C). Chipsets for two established wireless protocols—802.11 wireless LAN and Bluetooth—were considered, but proved not to be the strongest candidates for measurement purposes.

Intersil Corporation is the producer of the Prism II chipset, an 802.11 WLAN-compliant chipset that transmits up to 11 Megabits/second using Direct Sequence Spread Spectrum (DSSS) signaling in the ISM band. Intersil manufactures and sells evaluation boards packaged as PCMCIA cards for laptop computers, allowing a certain level of mobility. However, while these boards function perfectly as communication units, altering them for propagation experiments seemed beyond the schedule and scope of the project. Bluetooth, which uses Frequency Hopped Spread Spectrum at data rates up to 1 Mbit/s, was also considered. Many companies including Ericsson and National Semiconductor offer chipsets. However, a similar problem as the Prism II exists in that it is difficult to alter the hardware and software of the evaluation boards for propagation measurements.

There are also many commercial spread spectrum transceivers on the market that were considered for the studies. Xetron Corporation sells the Hummingbird 900 MHz spread spectrum transceiver and Linx Technologies sells the Linx. While both of these transmitters provide spread spectrum communication, wideband measurements would require a spectrum analyzer on the receiver, thereby limiting the necessary siting mobility previously discussed.

3.2 Internal Draper Hardware: DWN Transceiver

Because of the lack of mobility or measurement capabilities in commercial hardware, the investigation into measurement equipment became focused on internal Draper hardware. The Draper Wireless Network (DWN) transceiver is a small, programmable unit that sends continuous wave (CW) or binary frequency-shift keying (FSK) modulated waveforms across an approximately 100 MHz bandwidth in the ISM band. It was originally designed as a data transceiver for a wireless local shipboard network that was used for communication between remote sensors and several access points.

The DWN transceiver seemed to be the optimal solution in the hardware investigation for numerous reasons:

- 1) Measurement flexibility. With an on-board microprocessor, the transceiver can be programmed to any carrier frequency within its bandwidth. Additionally, any binary data stream can be transmitted. In receiver mode, the transceiver has the capability to measure and store average received power.

- 2) Siting flexibility. The compactness of the transceiver (it measures ~2.5" by 3.5") renders it extremely mobile. It can therefore be placed in various configurations and locations.
- 3) Primary Draper information sources. The DWN transceiver was fully designed internally by communication systems and RF engineers at Draper Laboratory. Therefore, any questions of usage or alterations can be directed first-hand to the designers of the board.
- 4) Upgrade capability. As previously mentioned, a secondary goal of the project was to find hardware that could be utilized not only as a measuring/modeling system, but that could be upgraded to a mobile data communication network. The DWN transceiver has such capability.

For these reasons, the transceiver was selected as the primary hardware centerpiece of the propagation modeling equipment. Design specifications for the DWN board can be found in Table 3-1.

FEATURE	SPECIFICATION
Data Rate	57.6 kilobits/second
Center Frequency	2.45 GHz
Bandwidth	195 MHz (2290 – 2485 MHz)
Number of channels across bandwidth	140 channels
Modulation Type	f_0 +/- 50 kHz Binary FSK or CW
Synthesizer Frequency Hop Time	\leq 1.0 millisecond
Transmit Power Level	\sim 1 milliwatt (mW)
Antenna Polarization	Vertical
Voltage	3.3 Volts

Table 3-1: DWN Transceiver specifications.

3.3 DWN Transceiver Design

The DWN transceiver consists of two primary sections: the microprocessor and the radio unit, both on a single board. The programmability of the transceiver is derived from the microprocessor section. It contains a Motorola 68HC12A4 microprocessor, a 16-bit 8-MHz microprocessor with various on-chip peripheral modules, including two serial communication interfaces, an 8-bit analog-to-digital converter, 1024 bytes of RAM, and a 4 Kbyte EPROM. The ease of usage of the HC12, along with its peripherals, renders the transceiver an excellent measurement system for propagation modeling.

The other side of the transceiver board contains the radio section. This functions both as a transmitter and receiver, depending on how the microprocessor is programmed. Various control signals from the HC12 determine the functionality of the radio section. Figures 3-1 and 3-2 are block diagrams detailing transceiver functionality in transmit and receive modes, respectively. Both figures show the essential control signals from the HC12 needed for proper radio functionality.

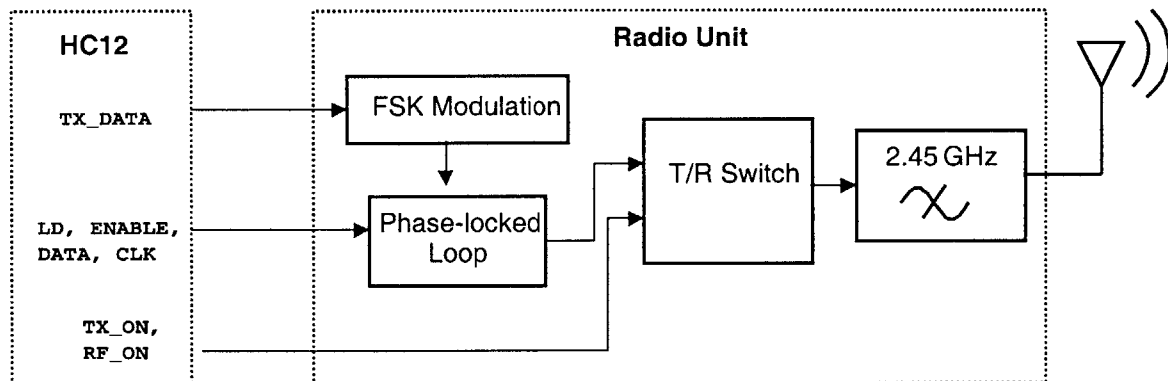


Figure 3-1: Block diagram of DWN Transceiver in transmit mode.

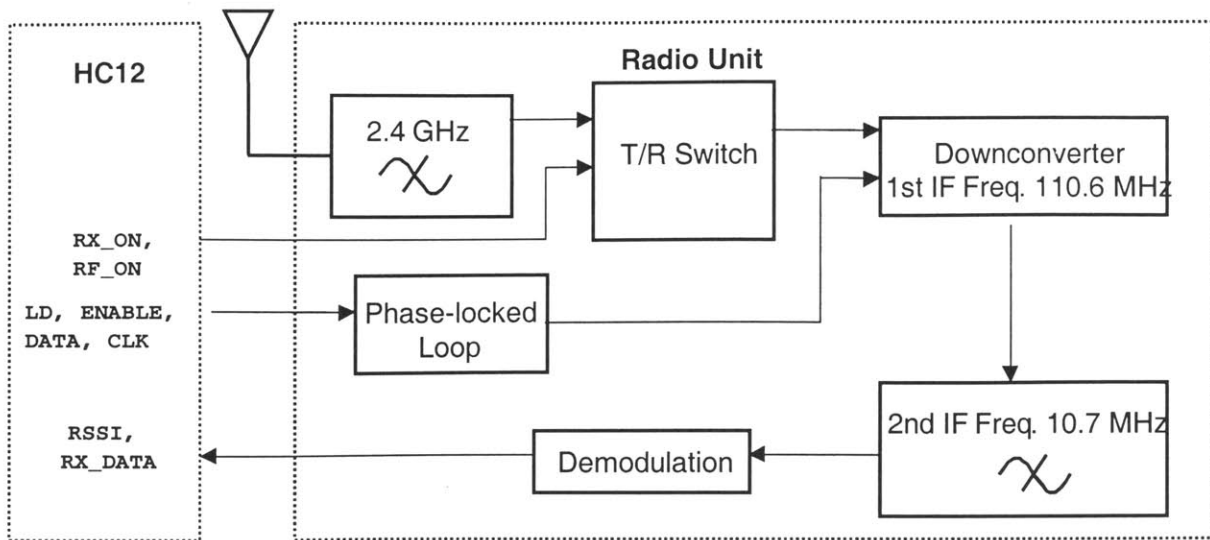


Figure 3-2: Block diagram of DWN Transceiver in receive mode.

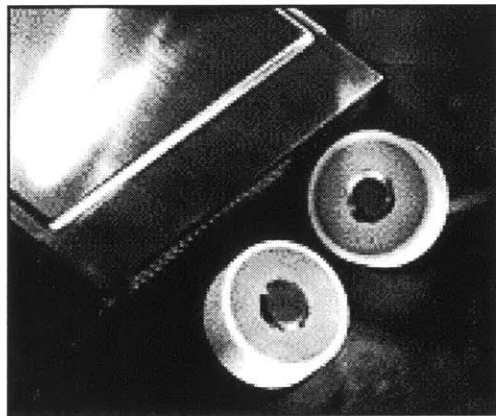


Figure 3-3: Toko antennas.

The antennas used in the measurement system are vertically-polarized, dielectrically-loaded patch antennas produced by Toko America, Inc. They can be seen in Figure 3-3. The bandwidth of the antennas is 100 MHz centered at 2.45 GHz. See Chapter 4 for further discussion concerning antenna characteristics and Appendix D for antenna data sheets.

3.4 Software Design

The layout of the microprocessor section contains a 6-pin port used to program the HC12. This allows programming to occur without detaching the microprocessor from the board. All software is written using Imagecraft's ICC12 C compiler and development environment for Motorola HC12 microcontrollers. Additionally, the Ax-BDM12 background debug module by Axiom is used for the actual board programming. The module connects to a PC via parallel port and programs the EPROM of the HC12 on the transceiver through the aforementioned 6-pin port.

3.4.1 Transmitter

Propagation measurements were performed in this project using two DWN transceivers: one in transmit mode and the other in receive mode. The transmitter is programmed to send either a CW or FSK-modulated waveform. Because the received power measured at the receiver is not dependent upon the transmitted digital data stream, the transmitter operation is simple. It consists of setting certain switches in software in order for the transceiver to operate in the correct mode. Then, a channel center frequency is selected and arbitrary data is generated to send.

Setting the proper switches for the transceiver to operate in transmit mode involves writing the correct signals to Port H, the microprocessor I/O port connected directly to switches on the radio side of the board. More specifically, the hexadecimal value 0x05 must be assigned to Port H, thereby setting signals TX_ON and RF_ON high.

To select a channel frequency, the HC12 is programmed to assign values to certain variables used by the frequency synthesizer on the radio side of the transceiver. The operating frequency of the radio is determined by Equation 3.1:

$$f = [P * B + A] * f_{ref} / R \quad (3.1)$$

where f_{ref} is the frequency of the reference oscillator, or 10.0000 MHz. For example, to transmit at 2.400 GHz, $P = 32$, $R = 17$, $A = 16$, and $B = 127$. Since P and R are kept constant, the only variables to select are A and B . This is done in software by creating large arrays of values for A and B and then selecting whichever values were needed to synthesize a given frequency.

Finally, it was necessary to program the microprocessor to generate data. Taking advantage of one of the HC12's peripheral modules, data was generated using a serial communications interface (SCI) module, which allows full-duplex, asynchronous, NRZ serial communication. It accommodates either 8-bit or 9-bit data characters, and allows variable baud rates. Table 3-2 is a brief overview of the important registers used to control the SCI module.

REGISTER	DESCRIPTION
SCCR1	Control Register 1. Determines 8/9-bit mode, and enables/disables parity.
SCCR2	Control Register 2. Enables/disables SCI peripheral and software interrupt.
SCBDL	Baud Rate Register Low. Sets baud rate.
SCDRL	Data Register Low. Holds transmit data.
SCSR1	Status Register. Holds Transmit Data Register Empty (TDRE) flag

Table 3-2: SCI register descriptions.

The SCI transmission sequence begins with enabling the SCI and transmitter interrupts in software by assigning certain values to SCCR1, SCCR2, and SCBDL so that 8-bit, no parity transmission occurs with a baud rate of 57,600 kilobits/second. Then, the transmit data

register empty flag TDRE must be cleared and binary data can be written to SCDRL, a write-only buffer that holds data sent with a transmit shift register.

3.4.2 Receiver

The selection of the DWN transceiver as the primary hardware of the propagation modeling equipment was based on its capability to measure average received power across a certain bandwidth. This function is derived from the Motorola MC13156 wideband FM IF system on the radio section of the board (see Figure 3-1). This chip calculates average received power with a received signal strength indication (RSSI) signal, represented by a DC voltage on the radio. Therefore, to operate in receive mode and perform measurements, the DWN transceiver must be programmed to receive on the same channel as the transmitter sends, measure RSSI values, and then output these values via serial port to a laptop for storage. Figure 3-4 diagrams the data flow of information needed for the receiver to act as a measurement system.

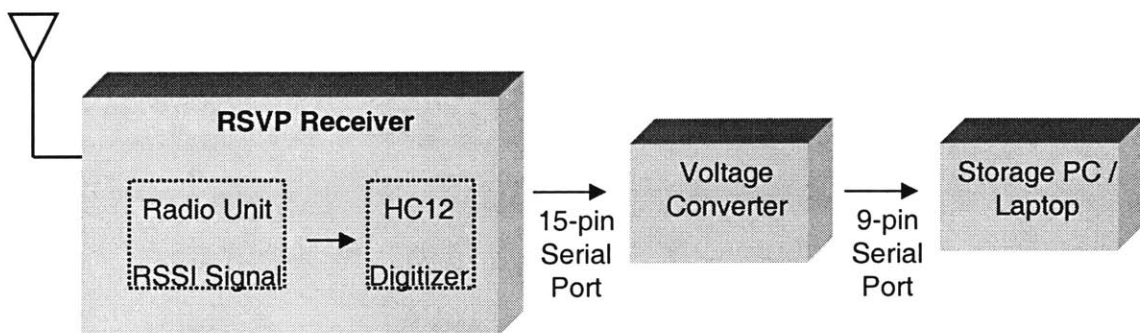


Figure 3-4: Receiver information flow.

Receive Configuration

Operating in receive mode begins with setting the proper switches on the I/O Port H. This involves assigning a hexadecimal value of 0x06 to the port. The receiver must also be configured to receive on the same channel that the transmitter sends. As previously mentioned, this involves assigning certain values to the variables *A* and *B* in Equation 3.1. It is important to note that the receiver was always programmed to receive at 110.588 MHz lower than the frequency at which the transmitter communicates, as the received signal is downconverted to this on-board IF frequency.

Digitizing RSSI

For the purposes of propagation modeling, the receiver must also have the capability to read the RSSI signal and translate the DC voltage into useful data. Thus, the signal must be digitized using the microprocessor's analog-to-digital converter (ATD) peripheral module, an 8-channel, 8-bit multiplexed-input converter. Table 3-3 is a brief overview of the important registers used to control the SCI module.

REGISTER	DESCRIPTION
ATDCTL2	ATD Control Register 2. Enables/disables ATD peripheral and software interrupt.
ATDCTL4	ATD Control Register 4. Sets ATD sample time.
ATDCTL5	ATD Control Register 5. Sets ATD conversion mode.
ADROH	ATD Result Register 0. Read-only register containing result from conversion.

Table 3-3: ATD register descriptions.

Programming the HC12 to perform conversions of the RSSI signal involves configuring the ATD module correctly. Values are assigned to ATDCTL2, ATDCTL4, and ATDCTL5 in

order to perform one 8-channel conversion in 486 microseconds with sequential channel conversions.

Real-Time Interrupt

As will be discussed in subsequent chapters, it is imperative to know and be able to select the exact sampling rate of the ATD peripheral module in the receiver. This operation is controlled with a real-time interrupt, which is a function of the HC12 clock module. Functionality of this interrupt is determined by the time-out period of a software interrupt. By assigning the correct bit value associated with the desired sampling rate, it is possible to control how often the receiver samples using the ATD peripheral.

The time-out period of the `RTICTL` is determined by Equation 3.2:

$$period = \frac{1}{M - clock / 2^x} \quad (3.2)$$

where M-clock is half the frequency of the main HC12 system clock and 2^x is the M-clock divisor. Since the system clock is 14.7456 MHz, M-clock is 7.3728 MHz. The M-clock divisor is determined by the three lower bits of `RTICTL`, which are termed the real-time interrupt rate select bits `RTR[2:0]`. These three bits are assigned a hexadecimal value of 0x100 in the receiver, which corresponds to an M-clock divisor of 2^{16} . As such, the time-out period is ~0.0089 seconds, or one cycle every 112.5 seconds. More discussion of the selection of this sampling rate can be found in Chapter 4.

Data Storage

In order to store the received digital RSSI values, they must be output to a laptop via its serial port. Because of the peripheral modules of the HC12, this simply involves writing each RSSI sample to a second serial port interface (SCI). This procedure is similar to binary data generation using the SCI of the transmitter.

Because the SCI protocol is standard NRZ serial communication, the receiver data can be output directly to that of a serial port on a laptop computer. However, the $\pm 3.3\text{V}$ rail-to-rail swing of the data from the receiver cannot be properly read by a laptop's serial port, whose rail-to-rail swing is around $\pm 15\text{V}$. Therefore, the voltage level is converted using an LTC1386, a 3.3V low-power EIA/TIA56 transceiver whose outputs can be forced to $\pm 15\text{V}$. The output data from the LTC1386 can then be fed into the serial port of a laptop.

3.5 Packaging

Providing a suitable package for the boards was necessary, both for ease of mobility and convenience of operation. Figure 3-5 shows the receiver board in its package, along with a laptop computer and a package for the voltage level conversion circuitry. The transmitter is packaged in a similar manner as the receiver, though in a slightly larger case to leave room for a power amplifier if one is desired.

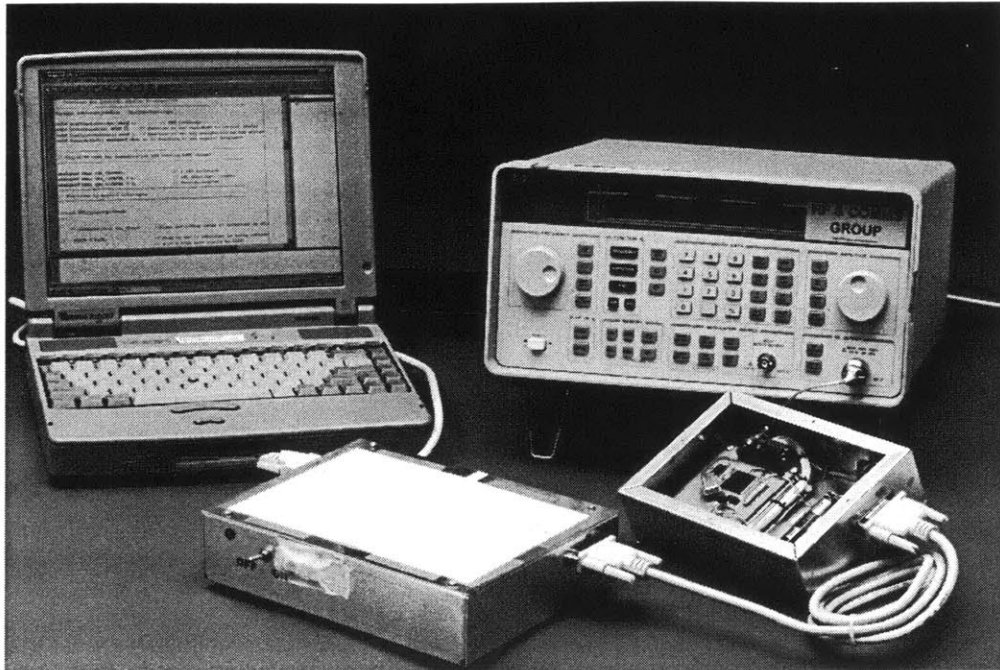


Figure 3-5: Receiver instrument setup. The DWN transceiver is seen on the lower right, and the voltage converter unit is on the lower left of the photograph.

While packaging the transceivers, two key issues were taken into consideration: size and power supply. Figure 3-5 clearly shows that the packages were constructed as small as possible to fit the transceiver, as well as a DC power source. Size is an important issue in this project, as the measurement system must mimic any possible mobile network siting situation. Furthermore, mobile measurement units are much easier to use in field experiments than larger network analyzers.

An additional packaging concern was the issue of providing a power source. Since the DWN transceivers draw approximately 45-50 mA and the radio requires a power source of at least 3.3V, using 3 commercial AA batteries provides sufficient power. Three AA batteries provide 4.5V as well as 500 mA-hours, therefore giving the transceivers an approximately ten hour lifetime on a single set of batteries.

One design issue that surfaced during receiver calibration was that the microprocessor section of the board was not regulated. This led to problems with a fluctuating RSSI value depending on battery voltage, thereby changing the calibration curve (see Chapter 4). The reason for this was not because the DC RSSI voltage was fluctuating; rather, the digital output values from the ATD changed depending on its voltage supply. The initial remedy to this problem was to place a small board with a Micrel MIC5205-3.3bm5 3.3V regulator between the battery and the transceiver. Since only the radio section contained an on-board regulator, this solution sought to regulate both the radio power supply, as well as the microprocessor power supply. However, the BDM12 debug module, which obtains its power from the power supply on the board, requires more power than provided by the regulated 3.3V supply. Therefore, instead of regulating the microprocessor power, it was necessary to regulate only the analog portion of the ATD module.

Chapter 4

Test Suite Characterization and Design

The previous chapter described the design and implementation of the DWN transceivers as large-scale and small-scale propagation modeling measurement systems. While the DWN transceivers have been used in other Draper Laboratory projects, their proper characterization for wireless channel modeling has never been performed. It was never necessary to identify the exact relationship between RSSI and received power, calculate the RSSI settling time, or understand the exact antenna gains and reception patterns.

Such information, however, is critical for the purposes of using DWN as a measurement system. This knowledge aids in understanding the process of how to extrapolate data measured with the transceivers into useful information for the wireless channel in question. Therefore, a thorough investigation of these issues was performed before field tests commenced. Furthermore, based on known theory and initial field measurements, it was necessary to formulate a test suite design in order to provide sufficient information to appropriately model a channel.

4.1 RSSI Characterization

The centerpiece of the transceiver measurement system is the RSSI signal. While RSSI values can be digitized on-board the receiver and then stored on a laptop computer, these values are unitless, numerical representations of a DC voltage. The recorded data says nothing of the exact value in decibels (dBm) or milliwatts (mW) of average power seen at the receiver. Therefore, proper pre-measurement characterization is needed in order to understand what the RSSI data actually means.

To perform such characterization, a calibrated Hewlett-Packard HP-E4433B signal generator was programmed to output a similar waveform as the transmitter, i.e. a 50 kHz FSK-modulated signal with a 58 kilobits/second symbol rate. The output of the signal generator was then connected directly into the receiver. Signal output power was varied from -20 dBm to -150 dBm, and then corresponding RSSI values were recorded.

This calibration procedure was performed for three test cases: room temperature (25° Celsius), 9° and 0° Celsius. The 9° and 0° temperature measurements were taken by placing the receiver and voltage converter both into a calibrated temperature chamber. Figure 4-1 shows a plot of RSSI values versus average received power in dBm.

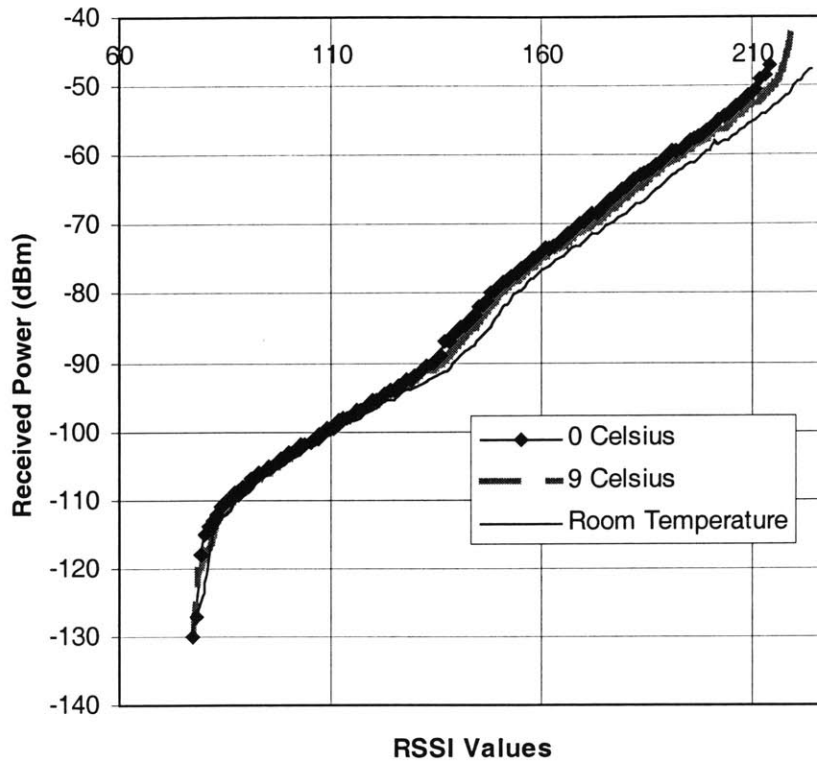


Figure 4-1: RSSI calibration curves.

Another necessary characterization of the RSSI values is its settling time, its time response to a change in received power. A requirement for propagation measurements is that the settling time of the RSSI loop is less than $1/3^{\text{rd}}$ of the measured correlation times. Otherwise, observed values would be determined by the measurement hardware and not the propagation environment. Characterization of settling time involved using the aforementioned signal generator. In addition, an oscilloscope was set up to measure the voltage of the receiver's RSSI signal. The output power of the signal generator was initially set at a given value, and then stepped either up or down to a second value. The oscilloscope was programmed in single-trigger mode to trigger once on a change in the RSSI DC voltage. Figures 4-2 and 4-3 demonstrate a rise and fall of the RSSI signal, respectively.

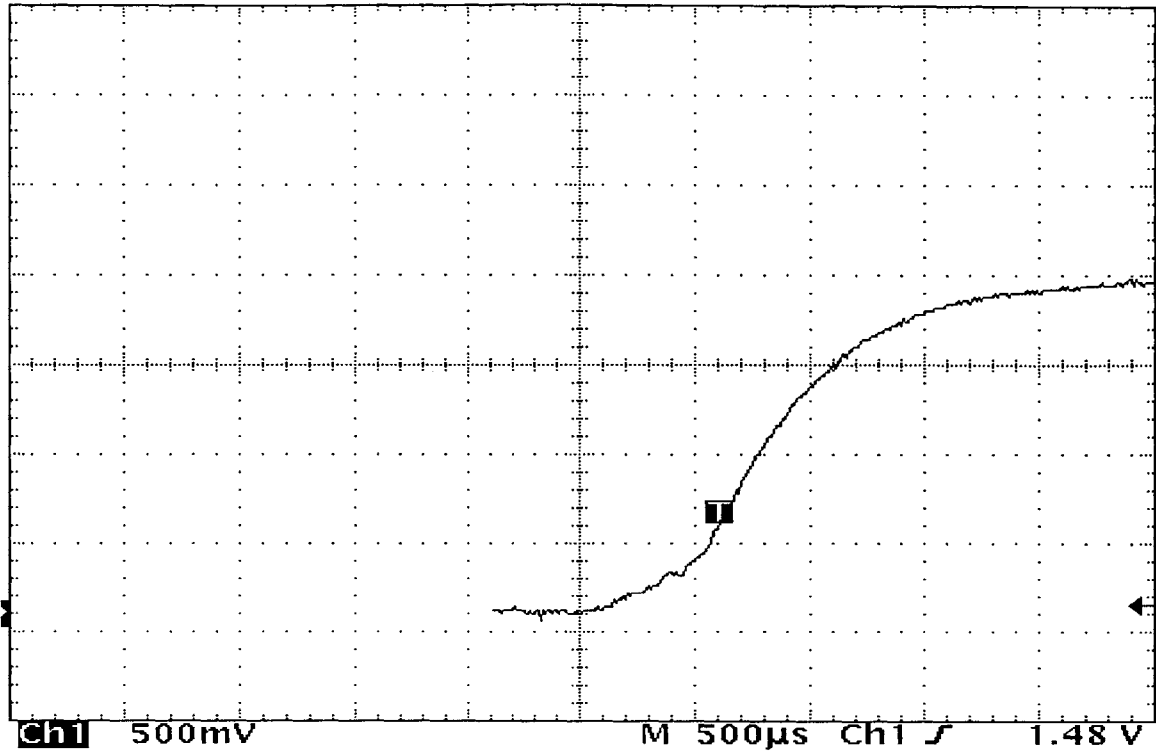


Figure 4-2: RSSI rise time.

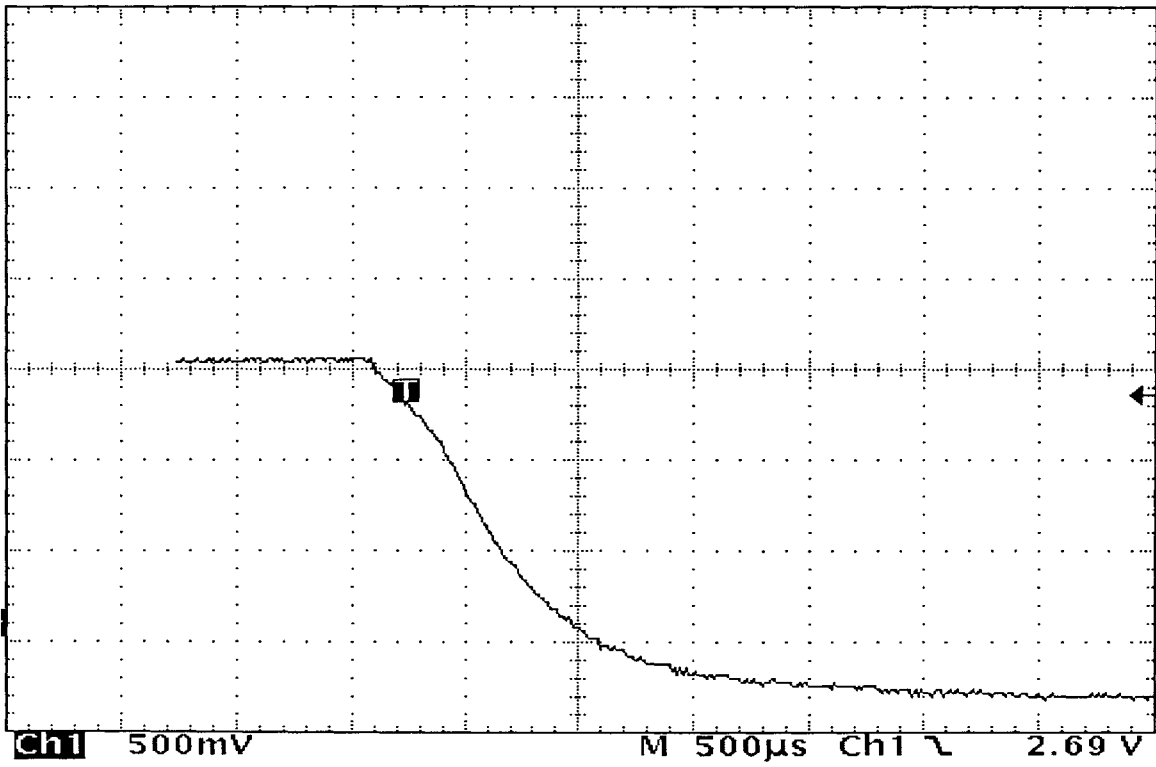


Figure 4-3: RSSI fall time.

In Figure 4-2, the output power of the signal generator was initially set at -120 dBm, then stepped up to -40 dBm. In Figure 4-3, it was stepped down from -120 dBm to -40 dBm. It can be seen from the figures that the settling time of the RSSI signal is approximately 2 ms.

4.2 Antenna Characterization

It is of utmost importance to understand what the received power values mean in the context of field measurements. Figure 4-4 is a diagram of an arbitrary field test configuration. In this figure, the translated RSSI signal in dBm represents the received power at point B relative to the output power at point A. To solve for the loss in dBm across any wireless channel, a simple equation based on Figure 4-4 can be used:

$$R_{xpower} = T_{xpower} + G_R + G_T - Loss_{Channel} \quad (4.1)$$

From Equation 4.1, to solve for channel loss, $L_{Channel}$, the three unknowns are T_{xpower} , G_T , and G_R . Using a spectrum analyzer, T_{xpower} of the transmitter was measured to be -1 dBm. Only the values of G_T and G_R for the DWN Toko antennas remained to be determined.

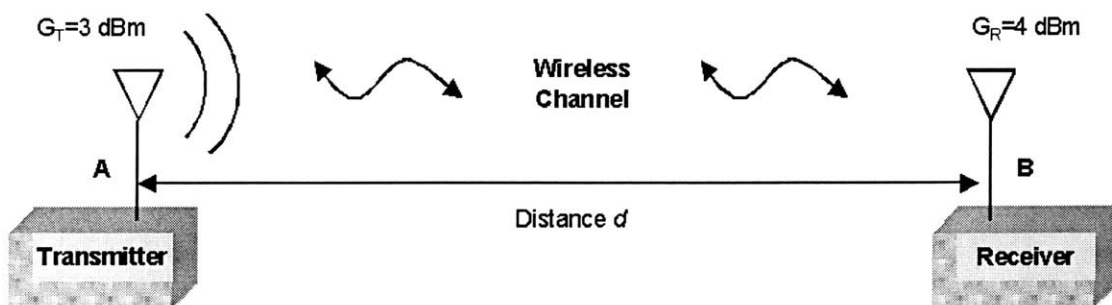


Figure 4-4: Generic field test configuration.

4.2.1 Antenna Resonance

Before investigating the gains of the Toko antennas, it is important to realize that these values vary across bandwidth. Furthermore, the response of no two antennas is exactly alike. Because the DWN transceivers have the capability to transmit across a frequency band of ~100 MHz, it is interesting to characterize this variation. Understanding this significantly reduces the error in using Equation 4.1 for calculating channel loss, as the gains of the antennas are known across the entire bandwidth and not just generalized to one numerical average.

Using an HP8753 network analyzer, the responses of three Toko antennas were recorded in order to find the resonance of each. Three antennas were characterized. The resonance of Toko antennas 1, 2, and 3 are 2.4, 2.37, and 2.34 GHz respectively.

4.2.2 Antenna Gain

To characterize the antenna gains, it was necessary to obtain calibrated antennas whose gains were already known. Two calibrated horn antennas, one produced by AEL Defense Corporation and the other by EMCO, were used for such characterization (See Appendix D for AEL and EMCO antenna datasheets). Both horn antennas are linearly polarized broadband antennas. The setup shown in Figure 4-5 was used to determine the gains of the Toko antennas.

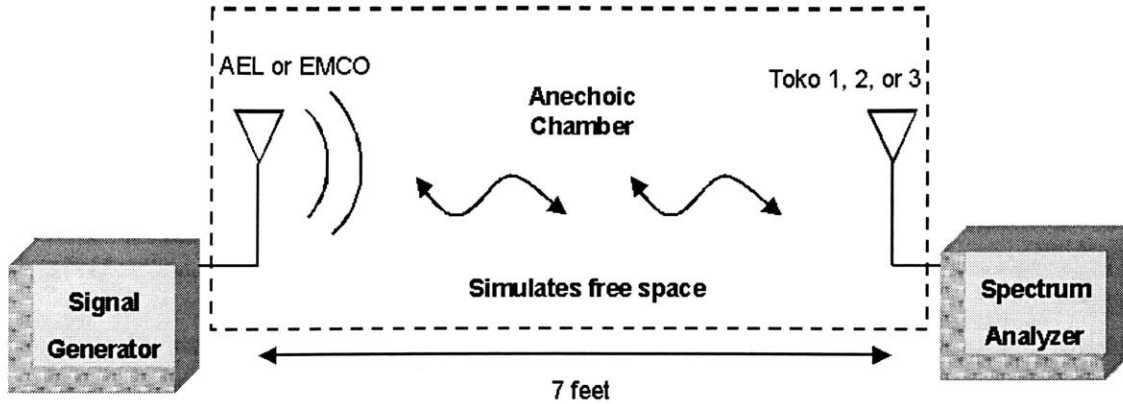


Figure 4-5: Toko antenna gain characterization setup.

It is important to note a few features from the setup shown in Figure 4-5:

- The signal generator output power was set to -1 dB to mimic the output of the transmitter. The frequency was varied between five different frequencies: 2 GHz, 2.34 GHz, 2.37 GHz, 2.4 GHz, and 3 GHz, representing the resonance of the three Toko antennas, as well as two additional frequencies.
- The antennas were placed seven feet apart in an 8-foot long anechoic chamber to simulate propagation through free space.
- Measurements were taken for all three Toko antennas using both the AEL and EMCO as transmit antennas. Toko gain values are averages of calculated gains using the two calibrated horns.
- Toko antennas were moved and rotated until a peak gain was realized for every measurement taken. It should be noted, however, that when oriented for vertical polarization, the received power drops 5 dB from peak antenna gain orientations.
- All cables connecting antennas to analyzers were calibrated out of the gain calculations.

Toko antenna gains were calculated using Equation 4.1. $L_{Channel}$ was calculated by using the free-space path loss equation:

$$FSLoss = 20 \log \left[\frac{4\pi d}{\lambda} \right] \quad (4.2)$$

Where $d = 7$ feet and λ is the wavelength of the transmitted signal. Table 4-1 is a summary of the recorded Toko gains at five frequencies.

FREQUENCY (GHz)	TOKO 1 (dB)	TOKO 2 (dB)	TOKO 3 (dB)
2	-18.54	-21.5	-25.2
2.34	-2.37	2.43	2.9
2.37	2.5	3.78	2.73
2.4	4	3.5	3.3
3	-5	-4.3	-2.18

Table 4-1: Summary of Toko gains.

4.3 Sampling Rate and Test Duration

Sampling rate was an important parameter to take into consideration, as measuring equipment should be able to sample the received power at the Nyquist rate associated with the highest Doppler shift caused by local movement [16]. Quick estimates showed that a sampling rate of 112.5 Hz was sufficient. At 2.4 GHz, Equation 2.24 shows that this rate allows the measurement system to measure channels with Doppler shifts of ~56 Hz, or velocities of up to 7.03 m/s. These values reach beyond those typically seen in the outdoor field studies necessary for this project. Furthermore, the RSSI settling time was shown to be ~2 ms. This is much faster than the sampling rate of the hardware, and therefore is not a concern.

In order to determine required test duration (i.e. length of time necessary for each measurement), initial “test runs” were performed to estimate coherence time. From [16],

the Doppler power spectrum $D(\lambda)$ is found by measuring amplitude fluctuations of a received CW signal in time. The magnitude square of the Fourier transform of these values gives $D(\lambda)$.

Measurements were performed in the courtyard of Draper Laboratory. The transmitter and receiver were placed atop bushes and separated by approximately 50 feet. RSSI was sampled for 20 minutes. Using the signal processing technique discussed above, RMS Doppler spread (see Equation 2.25) was calculated for windows of various time durations. The minimum Doppler spread calculated was found to be 0.3582, so the maximum coherence time is approximately the reciprocal of this value, or 5.5835 seconds. Therefore, in all field measurements, RSSI samples were recorded for at least 10 seconds, a time duration long enough to exceed the coherence times of most of the channels seen in field studies.

4.4 Test Suite Summary

Based on the characterizations of this chapter, a full test suite was designed whose features are summarized in Table 4-2.

FEATURE	SPECIFICATION
Data Rate	57.6 kilobits/second
Transmitted Signal	2.4 GHz CW
Antenna Polarization	Vertical
Transmitter Antenna Gain	4 dB
Receiver Antenna Gain	3.5 dB
Transmit Power level	-1 dB
RSSI Sampling Rate	112.5 Hz
Sampling Duration	≥ 10 seconds

Table 4-2: Hardware and test suite summary.

This test suite allows for narrowband sampling of RSSI. The measurement system therefore has the capability to perform large-scale path loss modeling, as well as some small-scale modeling.

Chapter 5

Large-Scale Deterministic Modeling: 2-ray Model

Once the propagation measurement system was fully developed, characterized, and designed, initial measurement efforts focused on performing large-scale deterministic modeling as described in Section 2.1. The reasoning behind this approach was that performing such experiments first would provide verification of experimental method. Using a deterministic physics-based analysis in simple network configurations, theoretical predictions of loss between transmitter and receiver can be made and tested in field measurements. If these predictions are reflected in measured data, it can be assumed that the hardware is properly functioning and measurement techniques are adequate.

As previously discussed, a deterministic approach to propagation modeling can only be used in environments with few obstructions and minimal local movement. To simulate such an environment, field experiments based on theory derived by Dolukhanov

[9] were performed at the center of MIT's Briggs Field. This location is a flat, open environment with no objects or obstructions, and is far enough away from local traffic or walkers that their movement is negligible in the measurements.

5.1 Attenuation Function Height Dependency

As developed in Chapter 2 and stated in Equation 2.19, the 2-ray model from [19] is dependent on calculating the attenuation function F :

$$F = \sqrt{1 + 2R \cos\left(\theta + \frac{4\pi h_t h_r}{\lambda d}\right) + R^2} \quad (5.1)$$

where F is a function of geometry defined in Chapter 2, as well as the surface complex reflection coefficient $\mathbf{R} = R e^{-i\theta}$. Maintaining a constant transmitter height h_t and separation distance d , it is a mathematically simple exercise to see that F passes through a number of maxima ($\cos(\theta + 4\pi h_t h_r / \lambda d) = 1$; $F = 1 + R$) and minima ($\cos(\theta + 4\pi h_t h_r / \lambda d) = -1$; $F = 1 - R$) with a varying h_r . Efforts of the initial propagation measurements performed on February 15, 2001 sought to verify this height dependency.

The measurement system configuration is diagrammed in Figure 5-1. The system transmitter height, h_t , and transmitter/receiver separation distance, d , were maintained at 1 and 10 meters, respectively. On the day the measurements were performed, the surface consisted of damp soil and grass. Calculations based on estimates from [21] yield R and θ values of 0.23 and 180° for such a surface and configuration. As seen in Figure 5-1, the measurements consisted of varying the height of the receiver, h_r .

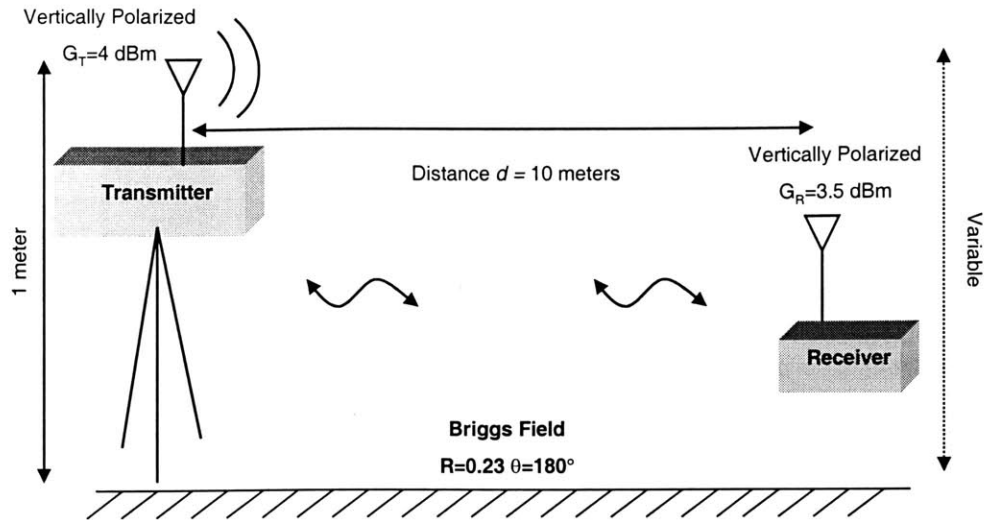


Figure 5-1: 2-ray height dependency measurement setup.

Based on these values, the theoretical attenuation function is periodic with respect to h_r with a period of 0.625 meters. Calculated theoretical values for the maximum and minimum values of F are 1.23 and 0.77, respectively. Dolukhanov [19] defines the adjusted free space path loss L' , taking into consideration the attenuation function, as:

$$L' = 20 \log \left(\frac{4\pi d}{\lambda} \right) - 20 \log F \quad \text{dB} \quad (5.2)$$

where d is transmitter/receiver separation distance, the first term represents free space path loss, and the second term is the loss contributed by the attenuation function F .

Path-loss measurements were performed across two periods of the theoretical F function, with receiver height varied from 0.3125 to 1.5625 meters in increments of 0.15625 meters. At each height, average received power was recorded over a 30-second interval. Figure 5-2 is a graph of measured path loss about a mean vs. distance. This data is overlaid atop the theoretical adjusted free space path loss defined in Equation 5.2. Measurements were taken twice in the same day and the sinusoidal behavior exhibited was both consistent and repeatable.

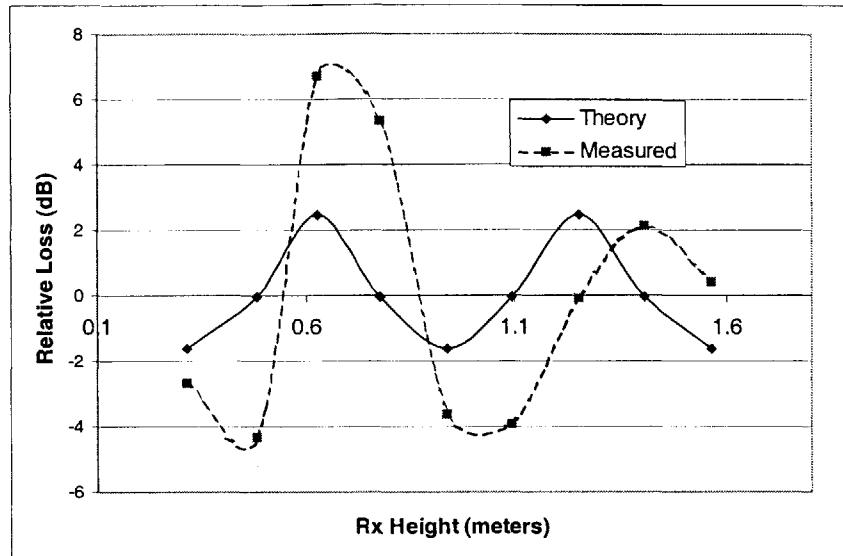


Figure 5-2: Measured and theoretical values of path loss about a mean vs. receiver antenna height.

From Figure 5-2, it should be noted that while the peak-to-peak variation in path loss may be different, there is a distinctly similar sinusoidal phenomenon seen in both theoretical and measured values. The slight phase offset between the measured and theoretical values can be attributed to a discrepancy between the estimated and actual value of the reflection coefficient R .

There also exists a discrepancy of on average 2 dB in amplitude between the maxima and minima of the estimated and measured values. The estimated values are derived by assuming that the surface is damp soil. The reflection coefficient R was recalculated assuming a reflecting surface of water. Under this assumption, the maximum and minimum of the theoretical values are increased by a little less than 2 dB, therefore explaining the discrepancy. The soil of the field was so wet that it acted essentially as water.

5.2 Attenuation Function Distance Dependency

With knowledge of the height dependency of the 2-ray model, the next step in deterministic propagation modeling is to investigate and understand the impact of d , the distance between the transmitter and receiver. A similar periodic behavior of F from Equation 5.1 can be seen with respect to d as that seen with respect to h_r in the previous section. That is, with h_t and h_r held constant, the attenuation function passes through numerous maxima and minima versus d . Figure 5-3 is a plot of such variation in the general case without defined R and θ values. It is important to note that in this figure there is a certain distance d_{max} over which periodicity occurs. Beyond this distance, the grazing angle of the reflected ray becomes small, $\theta + 4\pi h_t h_r / \lambda r$ from Equation 5.1 approaches π , and F decreases tending to zero in the limit [19].

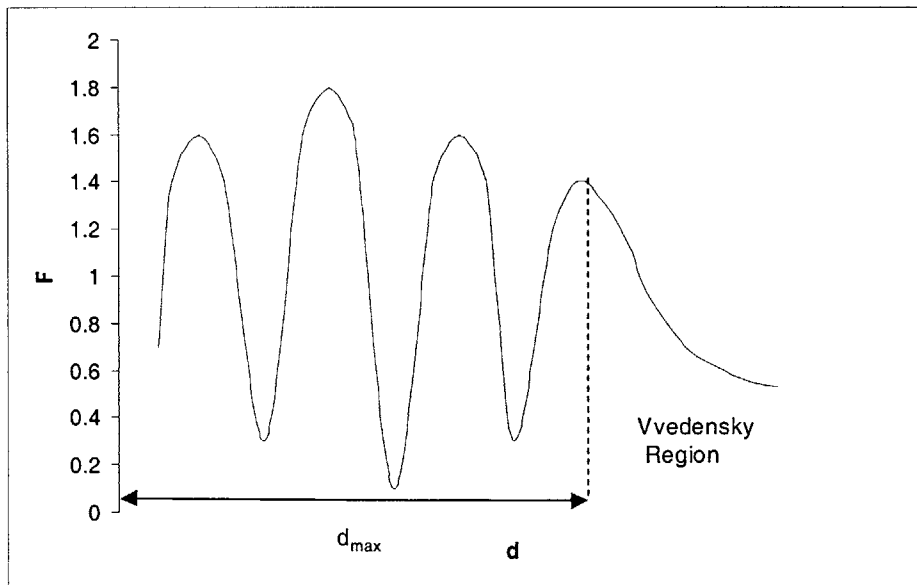


Figure 5-3: General case of attenuation function vs. distance (m) [19].

A second set of propagation experiments was designed around the relationship between the attenuation function F and the distance d exhibited in Figure 5-3. The measurement configuration was similar to that shown in Figure 5-1. However, keeping h_t and h_r fixed at 1 meter each, the distance d was steadily increased from 5 to 150 meters. These measurements were performed at Briggs Field on February 26, 2001. The surface consisted of damp soil and grass with similar R and θ values as seen in section 5.1.

The calculated attenuation function F for the described geometry and surface conditions is plotted in Figure 5-4. One important concept to note is that R and θ , the amplitude and phase of the reflection coefficient \mathbf{R} , are not constant over distance d . \mathbf{R} is not only dependent on the reflective surface, but also the grazing angle at which the reflected ray hits.

The data points shown in Figure 5-4 indicate experimentally measured values. The absolute maxima and minima of the attenuation function F may not be shown. However, it is still clear that the values of r at which measurements were taken yield two approximate attenuation function maxima and one minimum. Most measurements extended into the region past d_{max} , at which the attenuation function becomes asymptotic towards a certain value. This distance is seen to be approximately 35 meters, a value similar to the approximate estimated value in [19] of $4h_t h_r / \lambda = 32$ meters.

Figure 5-5 is a plot of the measured path loss values versus distance d overlaid atop the theoretical adjusted path loss values calculated with Equation 5.2. The similarity between the two plots is quite obvious, and is most clearly seen in the peak of both plots at the distance $d=15$ meters. The results shown in Figure 5-5 further verify the validity of the 2-ray model developed in [19] and [11].

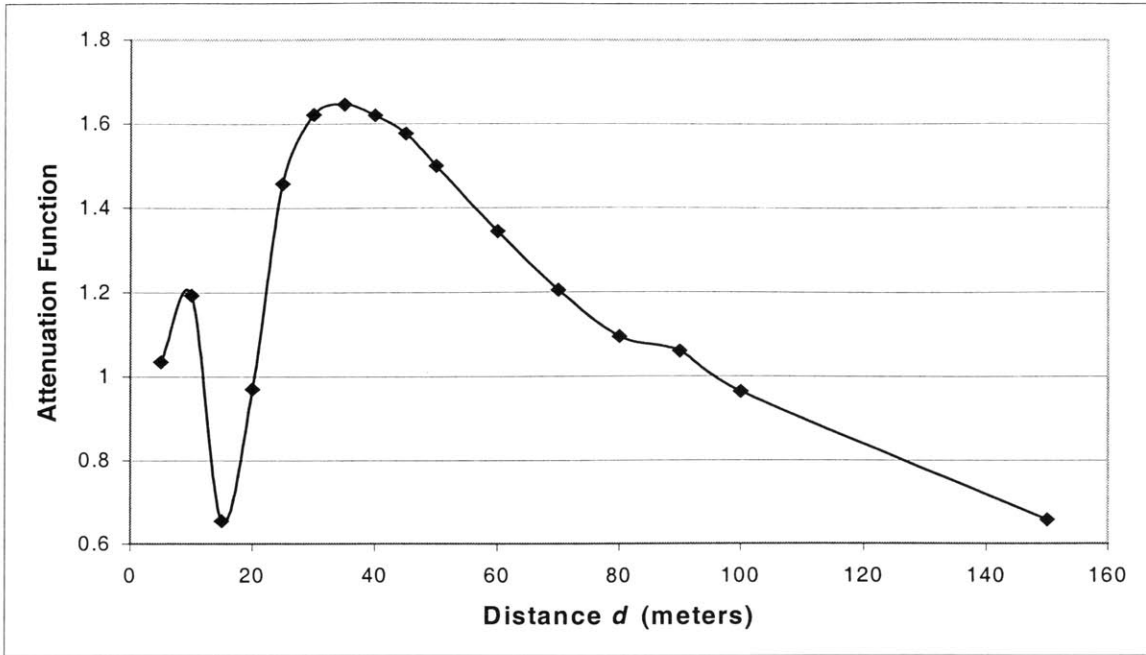


Figure 5-4: Briggs field calculated attenuation function vs. transmitter/receiver separation distance d .

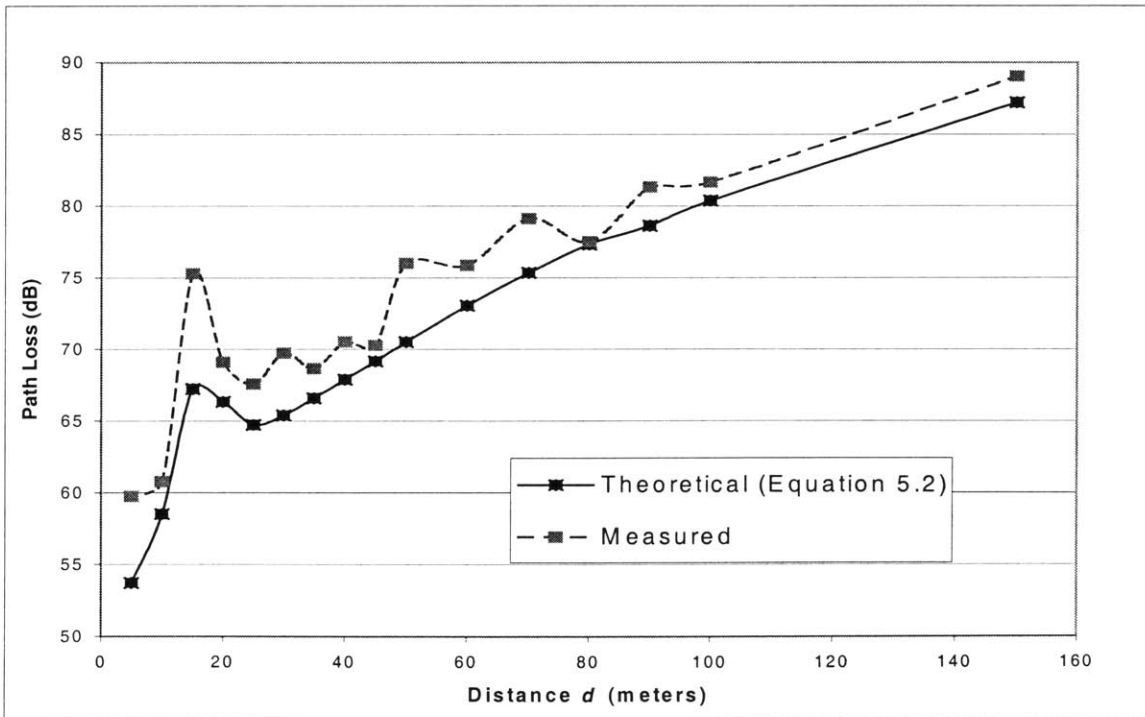


Figure 5-5: Briggs field measured and theoretical values for path loss vs. transmitter/receiver separation distance d .

5.3 Vvedensky Region

In Figure 5-3, there is a region after d_{max} labeled Vvedensky region. Equation 2.20 defined the attenuation function F for small grazing angles as:

$$F = 2 \left| \sin \frac{2\pi h_t h_r}{\lambda d} \right| \quad (5.3)$$

Note that Equation 5.3 may be simplified whenever $\sin(x) \approx x$, or when $d \geq \frac{18h_t h_r}{\lambda}$ [19].

After this distance, $F = \frac{4\pi h_t h_r}{\lambda d}$. Rappaport [11] states that in this region, received power at a distance d from the transmitter can be expressed as:

$$P_r = P_t G_t G_r \frac{h_t^2 h_r^2}{d^4} \quad (5.4)$$

Equation 5.4 shows that received power falls off with a path loss exponent of 4.

Experiments were performed on March 20, 2001 at Briggs Field to investigate the Vvedensky region. Keeping h_t and h_r fixed at 1 and 0.1016 meters respectively, d was steadily increased from 5 to 110 meters. With these values, the theoretical Vvedensky region occurs at 14.63 meters. Figure 5-6 is a plot of the measured path loss values versus distance.

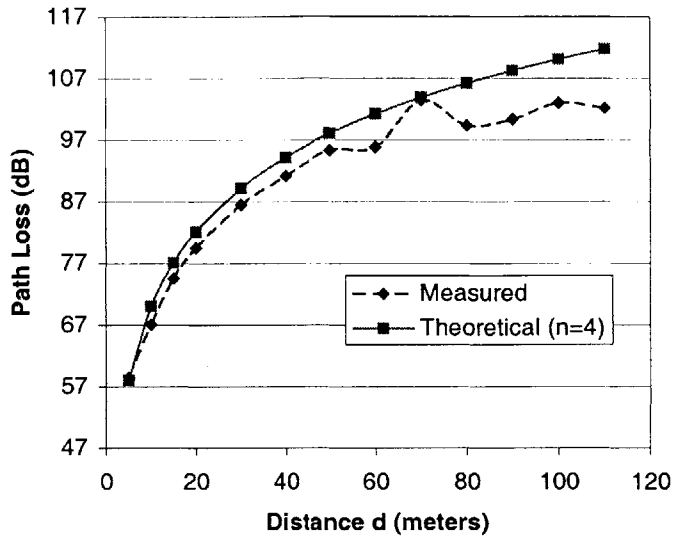


Figure 5-6: Measured values for path loss vs. transmitter/receiver separation distance in Vvedensky region; $h_t = 1$ meter, $h_r = 0.1016$ meters.

5.4 Deterministic Large-Scale Path Loss Model

In creating a model for large-scale path loss in simple settings, it has been shown in the previous sections that network geometry plays a large part in determining signal behavior. A model can therefore be partitioned into two distinct regions: a region (F region) where the attenuation function F significantly impacts received power, and the Vvedensky region. Figure 5-7 shows semi-log plots of the F region data set of Section 5.2 and the Vvedensky data set of Section 5.3 overlaid atop theoretical plots with loss exponents of 2, 3, and 4. Using Equation 2.6, the average calculated loss exponent for the F region was found to be $n = 2.28$, while that in the Vvedensky region was $n = 3.863$. These values demonstrate that in simple settings, F-region propagation performs closely to that of free-space, while the measured n in the Vvedensky region validates Equation 5.4.

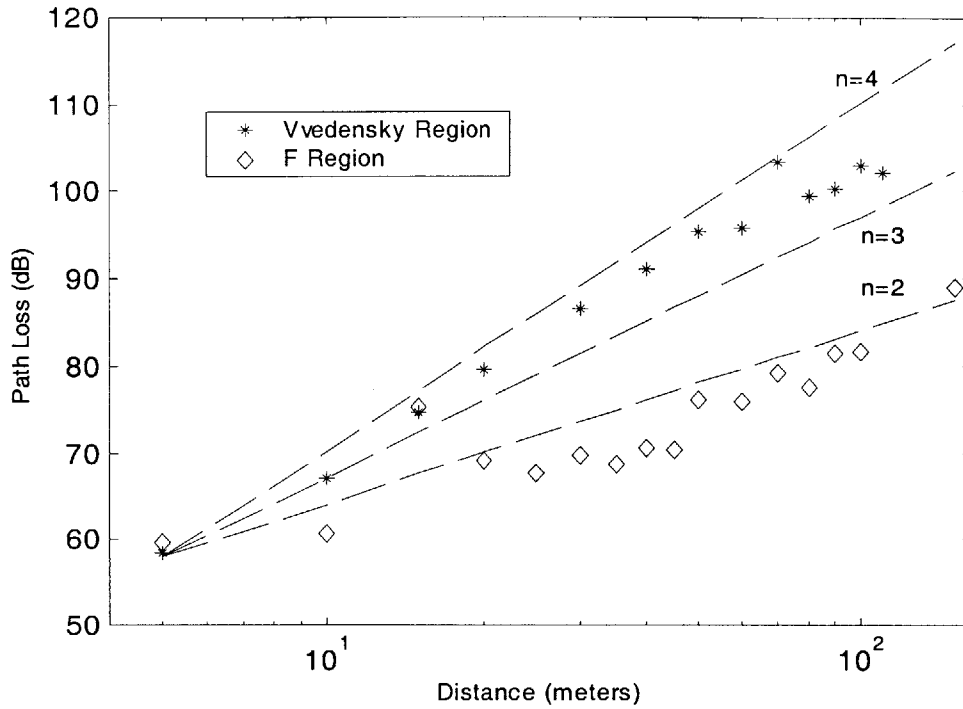


Figure 5-7: Measured F region and Vvedensky region path loss vs. distance.

A large-scale path loss model based on Equation 2.6 for simple settings based on field experiments can therefore be summarized as follows:

$$1) \text{ In the F region } (d \leq \frac{18h_t h_r}{\lambda}): L_p = L_0 + 10(2.28)\log_{10}(d / d_0) \quad (5.5)$$

$$2) \text{ In the Vvedensky region } (d \geq \frac{18h_t h_r}{\lambda}): L_p = L_0 + 10(3.87)\log_{10}(d / d_0) \quad (5.6)$$

It is important to note that while the $18h_t h_r / \lambda$ marker for signal behavior is quite specific, a general guideline is that at 2.4 GHz, low-ground (i.e. ≤ 1 meter) communication will often lie in the Vvedensky region.

Chapter 6

Small-Scale Statistical Modeling

In a flat, open environment, a deterministic approach can be used for propagation modeling. However, certain siting configurations for field deployable wireless control networks are located in much more complex environments where the basic 2-ray model may not apply. As discussed in Chapter 2, statistical analysis is a more realistic approach to modeling such settings. This project investigates small-scale propagation in three different complex siting situations:

- 1) Ground-based transmitter and receiver communicate through terrain with heavy foliage (e.g. trees, bushes, tall weeds).
- 2) Ground-based transmitter and receiver communicate through urban setting.
- 3) Elevated transmitter communicates to ground-based receiver through tree.

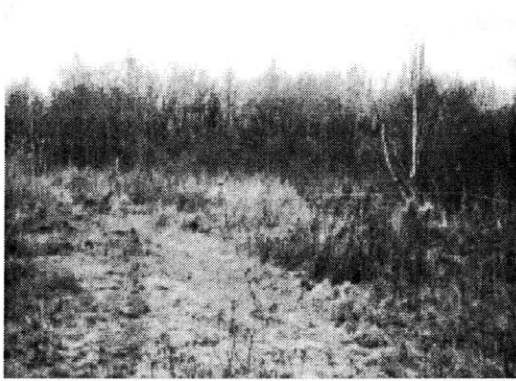
Both small-scale and large-scale phenomena are investigated. This chapter provides the small-scale investigation and the next chapter overviews large-scale results. Furthermore, the effects of the two phenomena are separated in order to understand their individual signal fading contributions.

6.1 Small-Scale Amplitude Distributions

In an environment with heavy foliage or vegetation, many objects small compared to the wavelength of the DWN transceiver exist, such as the branches of small bushes or trees. As a result, scattering—and therefore multipath fading—significantly impacts signal behavior. Field experiments were performed in various configurations and environments to investigate the distribution of the multipath-fading envelope.

The technique used for investigation involved placing the transmitter and receiver in realistic deployment configurations and then moving the receiver horizontally across a four-meter path perpendicular to the initial line-of-sight (LOS) direction. At intervals of seven inches, RSSI values were recorded. The four-meter distance is based on a suggestion found in [10] for a similar technique. Figure 6-1 shows pictures of the configurations investigated.

- *Ground-to-ground Through Vegetation.* Figure 6-1 (a) shows near-ground vegetation seen at Alewife Preserve in Cambridge, MA. Both transceivers were placed 1 meter from the ground separated with LOS by 40 meters (see Figure B-1 in Appendix B).
- *Ground-to-ground Urban Setting.* Figure 6-1 (b) shows the investigated urban setting. Both transceivers were placed 1 meter from the ground and were separated with LOS by 20 meters (see Figure B-4 in Appendix B).
- *Elevated-to-ground Through Tree.* Figure 6-1 (c) and (d) shows two types of trees investigated (Maple and Evergreen). The transmitter height h_t was approximately 3.5 meters high for tree experiments. In both experiments, the receiver was placed 1 meter above the ground on the other side of the tree (see Figures B-4 and B-8 in Appendix B).



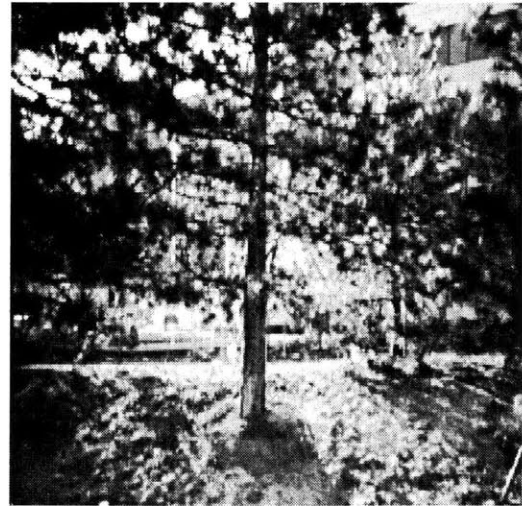
(a)



(b)



(c)



(d)

Figure 6-1: (a) Alewife Preserve—ground-to-ground vegetation (b) Vassar Street—ground-to-ground through urban setting (c) Maple Tree (d) Evergreen Tree.

Figure 6-2 shows histograms of the multipath-fading data recorded at Alewife Preserve and Vassar Street. Both charts are overlain atop probability distribution functions for Rayleigh, log-normal, and Ricean distributions. The parameters for the three theoretical distribution functions for each plot are calculated from the given environmental data. Results from the two tree measurements are not shown, as they exhibit similar behavior to the data collected from the other two environments (see Table A-1 in Appendix A for all measurements' distribution function parameters).

A quick glance at Figure 6-2 shows a close fit to the Ricean distribution function for both sets of data. Such a comparison seems appropriate, as it has been well documented in the literature [4, 11] that when a strong LOS path exists, the small-scale fading envelope appears Ricean.

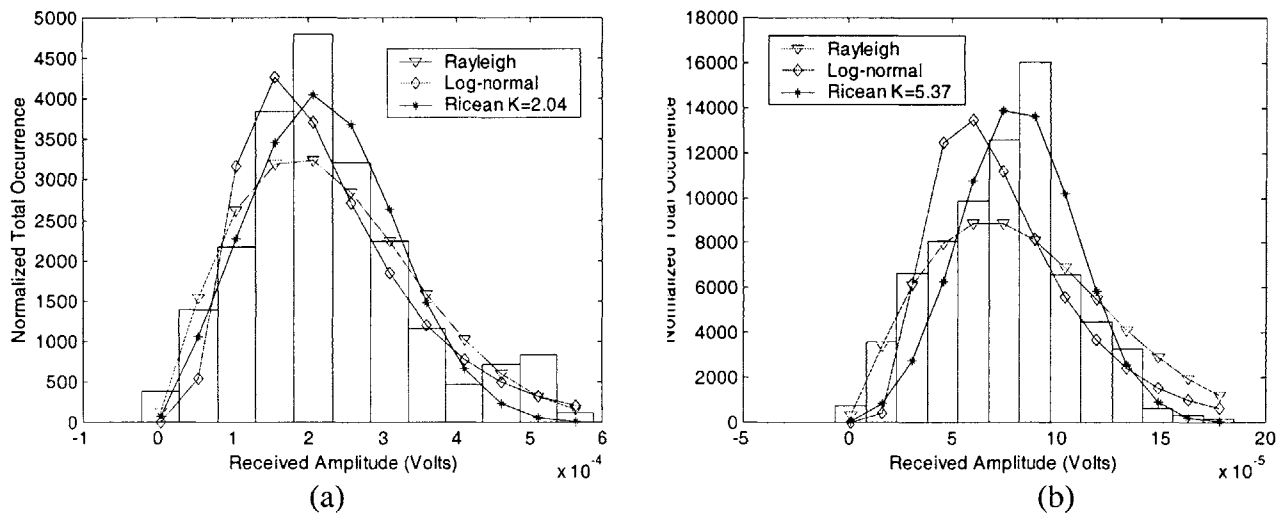


Figure 6-2: Histogram of small-scale amplitude measurements for (a) urban environment and (b) Alewife Preserve with thick ground vegetation. Theoretical PDFs with parameters based on environmental data are shown.

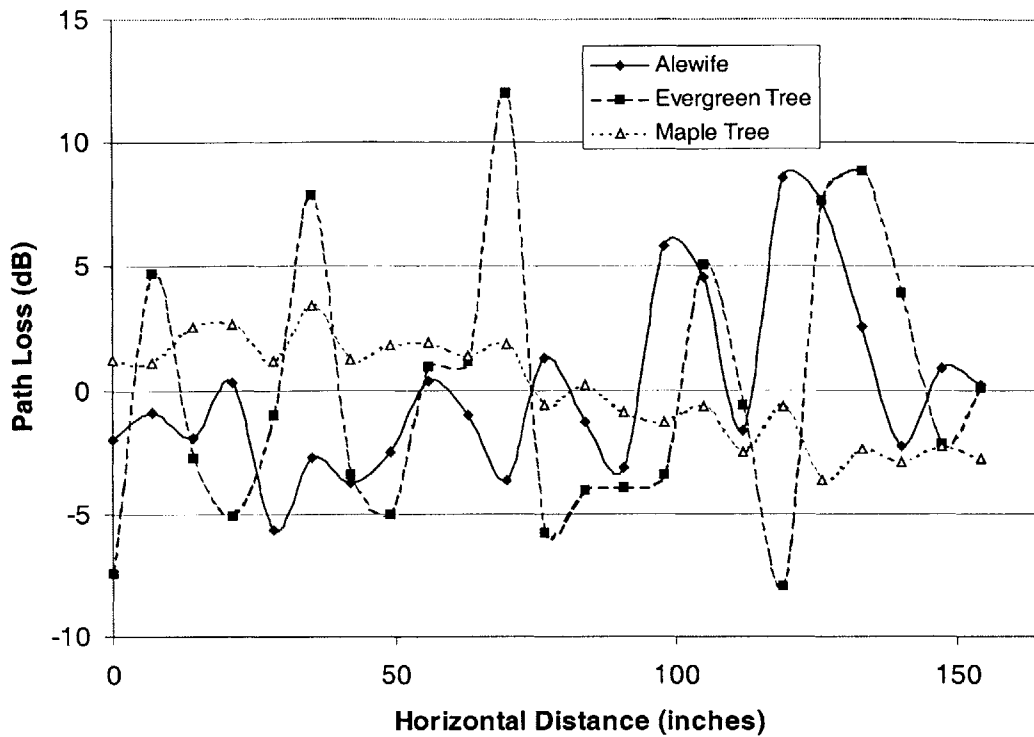


Figure 6-3: Path loss vs. horizontal distance for small-scale experiments.

Figure 6-3 is a plot of received path loss versus the horizontal distance across which the receiver was moved in the Alewife Preserve, Evergreen tree, and Maple tree experiments. It is clear that over a distance of only a few meters, path loss varies over a range as large as 15 dB.

One explanation for such small-scale variations lies in the theory of Fresnel zones. The size of local objects like cars and buildings in an environment largely control the strength of reflections. More specifically, if the size of an object is much larger than that of the first Fresnel zone, then reflections off of that object can be as significant as the LOS ray. The radius r_1 of the first Fresnel zone is given by Equation 6.1.

$$r_1 = \sqrt{\frac{\lambda d_1 d_2}{d_1 + d_2}} \quad (6.1)$$

where λ is the wavelength of the transmitted ray and d_1 and d_2 are the distances of the object from transmitter and receiver, respectively [11].

From Figure 6-3, the Evergreen tree experiment exhibited the largest fluctuations. These measurements were performed in an environment with buildings and cars nearby (see Figure B-4 in Appendix B). Using Equation 6.1 and the geometry of the physical surroundings, the first Fresnel zone has a radius of approximately 1.5 meters. Because the local reflectors (cars, buildings) are much larger than this dimension, reflections can be very significant. This explains the large fluctuations seen in Figure 6-3.

One other possibility for the large Evergreen tree fluctuations is that the receiver may have been moving in and out of Fresnel zones. Fresnel zones have the effect of alternately providing constructive and destructive interference to the total received signal [11]. This could explain the extreme peaks and valleys of the Evergreen tree experiment.

Another explanation for the variations in Figure 6-3 is that in multipath environments, path amplitudes and phases are altered significantly by various scatterers. An investigation was performed to see whether the effect of scattering played a part in the signal fluctuations of the Evergreen tree experiment. With transmitter and receiver heights and locations constant, branches of the tree were moved. This caused minimal effect on the received signal. Thus, the Fresnel zone explanation is a stronger reason for the Evergreen tree fluctuations.

The Alewife Preserve experiment also exhibited large fluctuations. Such variation can also be attributed to Fresnel zones, as a nearby metal fence may have acted as a strong reflector. In the Maple tree experiment, little fluctuation was seen. The smaller fluctuations in this experiment most likely come from the scattering discussed above.

6.2 Coherence Time and Doppler Spread

Another useful small-scale experiment for which the DWN transceiver was configured was to measure coherence time and Doppler spread in the manner of section 4.3. These parameters were investigated for an urban environment, thick vegetation, and trees with various transmitter/receiver siting configurations.

Figure 6-4 shows sample results of path loss variation in time, as well as Fourier transform Doppler spread measurements. Figure 6-4 (a) shows data from an urban environment (see figures in Appendix B.2). Transmitter and receiver were at fixed locations 50 meters apart and there was random movement of cars close to both units. Maximum power fluctuations caused by local movement of almost 10 dB can be seen in the time-domain plot. The bell-shaped Fourier transform plot shows the large Doppler spread B_D .

Figure 6-4 (b) shows data from a more rural environment with thick vegetation (see figures in Appendix B.1). Once again, transmitter and receiver were at fixed locations, but local movement consisted essentially of the vegetation blowing in a slight wind. With less time-domain variation of the received signal, the Fourier transform of magnitude measurements shows virtually no Doppler spread. Thus, the correlation between Doppler spread and local movement is clearly shown in Figure 6-4.

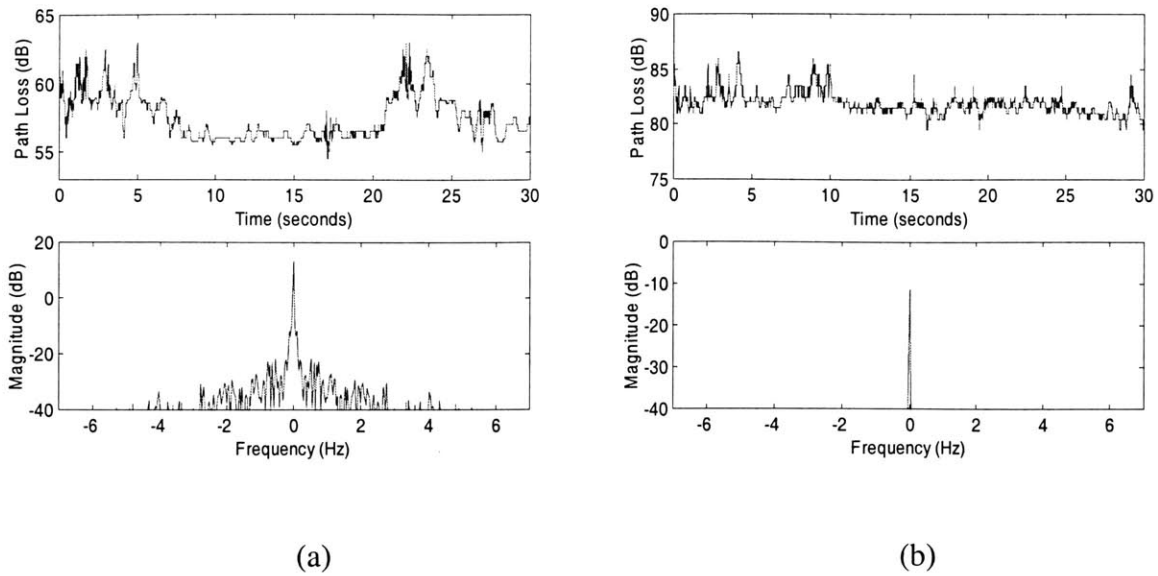


Figure 6-4: Time-domain and Fourier Transform Doppler spread plots for (a) urban environment and (b) rural environment with ground vegetation.

Table 6-1 summarizes Doppler spread B_{D-rms} and coherence time T_C measurements for various environments and configurations. All B_{D-rms} and T_C measurements are average values of multiple measurements taken with various separation distances between transmitter and receiver. The relationship $T_C \approx 1/B_{D-rms}$ as seen in Chapter 2 is used to calculate the value of T_C .

In the urban and rural environments, measurements were performed once with both transmitter and receiver 1 meter high and once with one unit placed directly on the ground. For the tree measurements, two siting configurations were investigated: one where the transmitter was hanging from a branch, and one where it was set firmly in the tree (see Figure B-8 in Appendix B). The purpose of this was to investigate the possible increase in Doppler spread caused by wind-induced movement of the transmitter.

LOCATION	ENVIRONMENT	SITING	B_{D-rms} (Hz)	T_C (s)
Vassar Street	Urban Street	Rx = 1m, Tx = 1m	1.067	0.937
Vassar Street	Urban Street	Rx = 1m, Tx = ground	2.348	0.426
Alewife Preserve	Thick Vegetation	Rx = 1m, Tx = 1m	0.617	1.621
Alewife Preserve	Thick Vegetation	Rx = ground, Tx = 1m	0.803	1.245
Along Vassar St.	Evergreen Tree	Rx = 1m, Tx = 3.5 m	0.482	2.075
Thorndike Park	Tree, No Foliage	Rx = 1m, Tx = hanging in tree	0.517	1.934
Thorndike Park	Tree, No Foliage	Rx = 1m, Tx = steady in tree	0.502	1.992

Table 6-1: Summary of Doppler spread and coherence time measurements.

From Table 6-1, there are some interesting observations to be considered. One obvious point is that clearly the urban environment with the greatest local movement shows larger Doppler spreads than those environments with less movement. This conclusion is similar to the one drawn from Figure 6-4.

Another interesting point to note is that in the urban and thick vegetation environments, Doppler spread is larger when one device is placed on the ground than when both transmitter and receiver are at heights of 1 meter. In the Alewife Preserve measurement with thick near-ground vegetation, one possible explanation for this is that when placed on the ground, a device is closer to the low-lying weeds and brush that act as scatterers. As such, there is a higher concentration of multipath rays on the device than when it is placed above these scatterers. Thus, any small movement can cause larger Doppler spreads because many multipath rays are affected.

Another explanation for the phenomenon of larger Doppler spreads with ground siting in both environments is the lack of a dominant LOS path. A well-accepted model for small-scale multipath in absence of a strong received LOS component obeys a Rayleigh distribution. When a device is sited on the ground in either environment, this decreases the dominance of the LOS path. As such, small movements in the environment

can cause the numerous OLOS paths from the Rayleigh distribution to change in phase, therefore causing larger Doppler spreads. When the devices are sited above ground, a stronger LOS component exists. Therefore, the Doppler spread is not as significantly altered as the changes in the OLOS paths are not as significant.

6.3 Small-Scale Fading System Design Implications

Depending upon the relationship between system parameters and channel parameters, transmitted signals exhibit different types of fading. Having taken measurements of Doppler spread and coherence time, channels can be characterized as exhibiting either fast or slow fading. In a fast fading channel, the symbol rate $1/T_s \approx B_s$ (where T_s is the symbol period) is less than the fading rate $1/T_c \approx B_D$. That is, $B_s < B_D$ and $T_s > T_c$. In a slow fading channel, the opposite is true: $B_s > B_D$ and $T_s < T_c$ [17].

Fast fading implies that the channel impulse response changes several times during the symbol duration. This causes random frequency modulation due to varying Doppler shifts [17], leading to signal distortion [11]. Such distortion results in a loss of SNR and irreducible error rates [26]. In a slow fading channel, errors can occur if the channel remains in a deep fade over the course of several symbol transmissions.

An entire thesis could be written investigating possible ways to combat the distortion caused by fast or slow fading. Multiple methods exist, including the use of different modulation techniques and various coding schemes. However, this project seeks to overview just a few communication system design options to combat small-scale fading.

One obvious method to combat fast-fading signal distortion is to change the signaling rate B_s of the communication system. For fast fading, $B_s < B_D$. This sets a lower limit

on B_s , required without suffering fast fading distortion. The exact factor by which B_s should exceed B_D depends on the signal modulation, receiver design, and required error rate [17]. Error correction codes are another method used to combat fast fading, as they reduce the required SNR [26].

It is clear from Figures 6-2 and 6-3 that, statistically, a signal can find itself in a deep fade of the channel. If slow fading exists, the duration of this fade can exist for over several transmitted symbols. In such a scenario, a large number of errors could occur in sequence or in bursts. An effective method to combat error bursts is to use an interleaver to spread the errors over many code words rather than just a few sequential words. See [11, 27, 28] for further insight into the design of interleavers and error correction codes.

Another method used to combat deep multipath fades is diversity. Diversity is defined as providing the receiver with two or more uncorrelated replicas of the signal. If a communication system can be designed using diversity, the probability that all components of the received signal are simultaneously in a deep multipath fade is reduced considerably [28]. One example is time diversity, which takes advantage of the coherence time of a channel. If the transmitter sends the same information in D different time slots separated by at least T_c , it is statistically likely that the D received signals are uncorrelated. Frequency diversity sends the same information on different carrier frequencies separated by at least the coherence bandwidth of the channel. It should be noted, however, that coherence bandwidth was not measured in this project. Finally, spatial diversity can also be used to combat deep fades. This involves using multiple receive antennas separated by a distance of at least 10λ [26] or the correlation distance of the fading. Figure 6-3 verifies the appropriateness of this method, as it is clear that the

channel behavior is uncorrelated across such spatial differences. In fact, Figure 6-3 suggests that spatial separation of as small as one wavelength may be helpful.

Chapter 7

Large-Scale Statistical Modeling

This chapter overviews the large-scale propagation modeling performed. Creating a large-scale statistical model involves finding a value for the path loss exponent n in Equation 2.6. Experiments were performed for the three environments listed in Section 6.1 to determine n , as well as the statistical variations about the mean for various transmitter and receiver distances (see Appendix B for detailed maps and photographs). This information is enough from which to extrapolate a large-scale path loss model.

For each large-scale experiment, receiver RSSI power values were measured as transmitter/receiver separation distance d was varied. From the previous chapter and Figure 6-3, it is known that at any given distance d , there are small-scale signal variations of up to 15 dB, if not more. To separate such variation from the larger scale variations with respect to distance, an averaging technique was used for large-scale measurements. At each distance d , both local maximum and minimum RSSI values were recorded and then averaged to determine an overall loss.

7.1 Ground-to-ground Through Vegetation

Ground-to-ground communication through vegetation was modeled at Alewife Preserve (see Appendix B.1). At each distance, transmitter and receiver heights h_t and h_r were initially set at 1 meter. The experiment was then repeated with the receiver placed on the ground. Figure 7-1 shows semi-log plots of the experimental data set overlaid atop theoretical plots with path loss exponents of 2, 3, and 4.

Using Equation 2.6, the average calculated loss exponent ($d_0 = 100\text{m}$) for $h_r = 1\text{ m}$ was $n = 3.42$ while when on the ground, $n = 3.87$. As in the 2-ray model of Chapters 2 and 5, when one device is on the ground, the loss exponent n is greater. However, unlike the 2-ray model, the difference in the value of n is not as significant. In both cases the vegetation changes the free-space loss exponent from 2 to approximately 3.5.

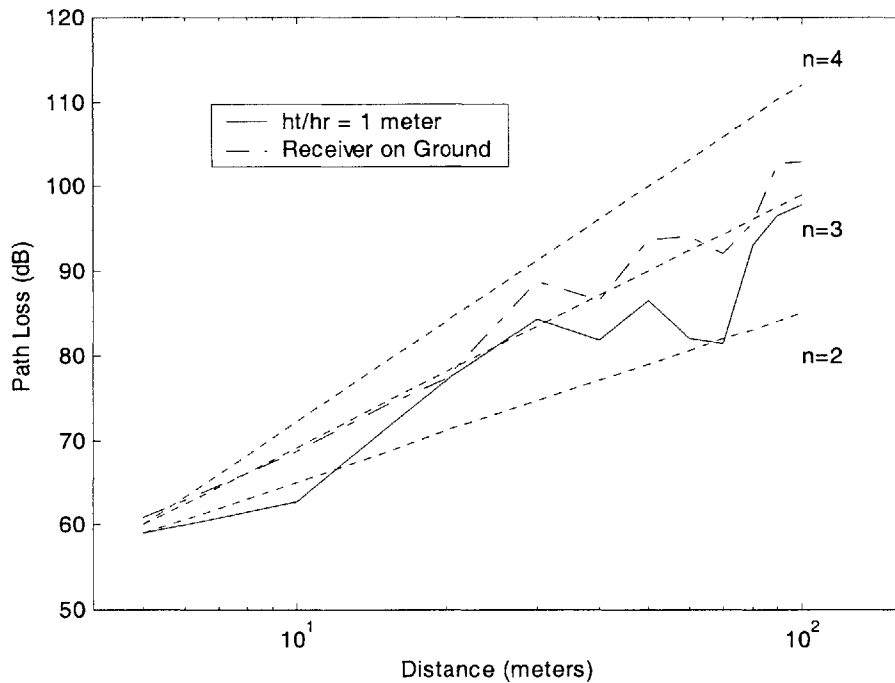


Figure 7-1: Path loss vs. distance at Alewife Preserve.

According to theory [17], at any distance d the path loss is a random variable having a log-normal distribution. Measurements were performed at Alewife Preserve to provide empirical proof of this behavior. For various separation distances d_0 , the transceivers were sited in arbitrary locations around the environment. Figure 7-2 shows a CDF of data samples performed with $d_0 = 20$ m. The samples are overlaid atop a log-normal CDF with parameters generated from the collected data. The plot represents a typical example of the type of distribution seen at other separation distances at Alewife Preserve, as well as similar measurements in other locations and environments. Indeed, the data does appear to be log-normally distributed.

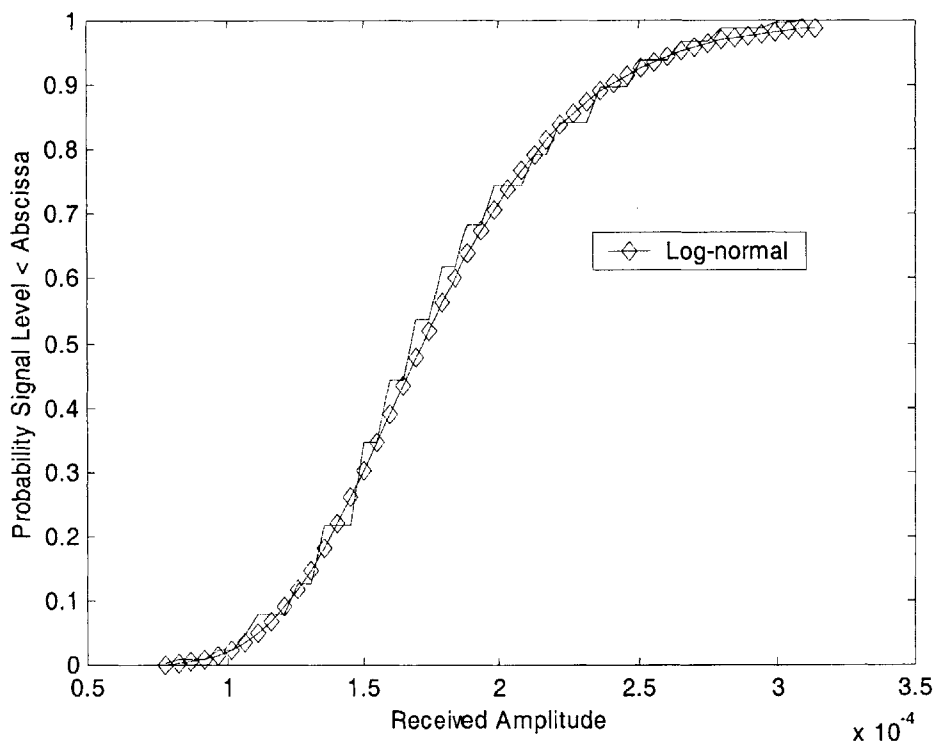


Figure 7-2: Example measured values for large-scale distribution at Alewife Preserve. The distribution is overlaid atop a log-normal CDF for comparison.

Based on Equation 2.6, a large-scale path loss model also includes a zero-mean Gaussian random variable X_σ to represent the fluctuation described above. A large-scale path loss model for the ground-to-ground through vegetation environment based on field experiments can therefore be summarized as follows:

$$1) \text{ For } h_r = 1 \text{ meter: } L_p = L_0 + 10(3.42)\log_{10}(d / d_0) + X_\sigma \quad (7.1)$$

$$2) \text{ For } h_r = 0: L_p = L_0 + 10(3.87)\log_{10}(d / d_0) + X_\sigma \quad (7.2)$$

where X_σ is a zero-mean Gaussian random variable with standard deviation 3.44 dB.

7.2 Urban Setting

Ground-to-ground urban propagation was measured along Vassar Street (see Appendix B.2). Measurements were performed in a similar manner as in section 7.1 using three different configurations. At each separation distance, transmitter and receiver heights h_t and h_r were originally set at 1 meter. The experiment was then repeated with the transmitter placed on the ground. Finally, a third experiment was performed with the AEL directional horn antenna (gain = 13 dB) on the receiver as opposed to the regular Toko antenna (gain = 3.5 dB). Transmitter and receiver heights were set to 1 meter for this third configuration. Figure 7-3 shows semi-log plots of the experimental data set overlaid atop theoretical plots with loss exponents of 2, 3, and 4.

The average calculated loss exponent ($d_0 = 150\text{m}$) for $h_t = 1 \text{ m}$ was $n = 3.03$ while when on the ground, $n = 3.18$. With the horn antenna configuration, $n = 2.8$. Once again, the near-ground propagation has a slightly higher value of n than when one device

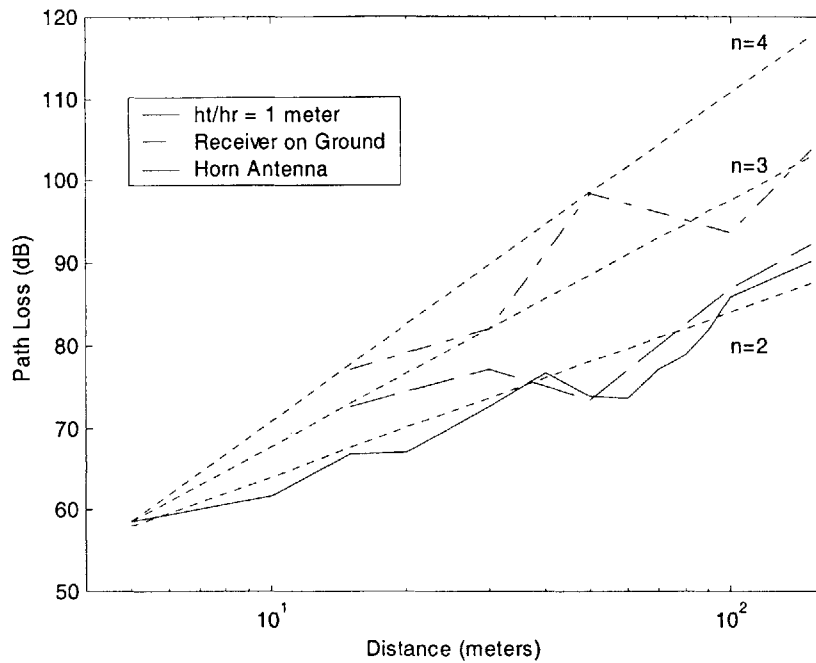


Figure 7-3: Path Loss vs. distance along Vassar Street.

is 1 meter off of the ground. This was seen in previous section as well in the vegetation measurements.

The horn antenna shows the smallest loss exponent n . This finding seems appropriate, as signals from a directional antenna do not see as many reflections and scatters from the local environment due to its more narrow beamwidth. Thus, distance-dependent signal degradation is smaller.

Experiments were also performed to investigate the standard deviation value of X_σ and it was found to be 4.66 dB. A large-scale path loss model for the ground-to-ground urban environment therefore is:

$$1) \text{ For } h_t = 1 \text{ meter: } L_p = L_0 + 10(3.03)\log_{10}(d / d_0) + X_\sigma \quad (7.3)$$

$$2) \text{ For } h_t = 0: L_p = L_0 + 10(3.18)\log_{10}(d / d_0) + X_\sigma \quad (7.4)$$

where X_σ is a zero-mean Gaussian random variable with average standard deviation 4.66.

It is important to mention that additional measurements were performed in the urban environment more for the purpose of siting testing rather than propagation measurements. A transmitter was placed atop the edge of a 40' tall parking garage at the end of Vassar Street, and the receiver at $h_r = 1$ meter was stepped slowly away from the garage along the street (see Figure B-7 in Appendix B). The value of the loss exponent for these measurements was $n = 2.11$. This value is very close to free space propagation. The difference in urban propagation when the transmitter is at a height of 1 meter as opposed to when it is atop a building most likely comes from the effect caused by lower-lying obstacles and reflectors. When the transmitter is at a height of 1 meter, there are many reflectors and diffractors in the local area that can cause signal loss. However, when atop a building, the transmitter is above many of these obstacles, thereby avoiding those same reflectors that would cause signal loss if the transmitter were closer to the ground.

7.3 Single Tree Propagation

This project was also extremely interested in signal propagation through a single tree and corresponding behavior changes as a result of foliage. No-foliage tree propagation measurements were performed on March 29th, 2001 at Thorndike Park (see Appendix B.3) in Arlington, MA. The transmitter height in the tree was $h_t = 3.5$ meters, while $h_r = 1$ meter.

The path loss models for the single tree experiment can be summarized as follows:

$$L_p = L_0 + 10(3.11)\log_{10}(d / d_0) + X_\sigma \quad (7.5)$$

where X_σ is a zero-mean Gaussian random variable with standard deviation of 4.69 dB.

7.4 Summary of Large-Scale Results

Table 7-1 is a summary of path loss exponents from all large-scale measurements performed. Please see Appendix A for a brief description of the tunnel measurements performed at MIT.

LOCATION	ENVIRONMENT	SITING	LOSS EXPONENT n
MIT Briggs Field	Open Field	Rx = Tx = 1m	2.28
MIT Briggs Field	Open Field	Rx = Tx = on ground	3.87
Alewife Preserve	Thick Vegetation	Rx = Tx = 1m	3.42
Alewife Preserve	Thick Vegetation	Rx = ground, Tx = 1m	3.87
Vassar Street	Urban	Rx = Tx = 1m	3.03
Vassar Street	Urban	Rx = 1m, Tx = ground	3.18
Vassar Street	Urban	Rx = 1m, Tx = atop building	2.11
Thorndike Park	Tree, No Foliage	Rx = 1m, Tx = steady in tree	3.11
MIT Tunnel	Tunnel	Rx = Tx = 1m	2.74

Table 7-1: Summary of large-scale results.

7.5 Large-Scale Fading System Design Implications

This chapter discussed the path loss values for various environments and configurations. Empirical measurements were made that show path loss ranging between exponent values of approximately d^2 and d^4 . Understanding these values and how a signal degrades over distance is important to the design of any communication system and the link level.

Before a system can be designed, estimates of link-level performance must be made. Creating a link budget—calculations and educated guesses of the gains and losses seen throughout the communications link—is often useful in forming such estimates. Knowledge of the path loss values for different environments enables more accurate link

budgets, as distance-dependent loss is one factor in the budget. The aircraft navigation system around which this project was created had an initial path loss estimate based on free space loss ($n=2$). The empirical data shows the inaccuracy of this assumption, and the link budget can now be altered.

Another system design parameter affected by knowledge of path loss in various environments is transmitter output power. In any communication system, understanding distance-dependent loss allows the designer to calculate what transmit power is necessary to achieve a given signal-to-noise ratio. The ability to detect a signal at the receiver with an acceptable error probability in the presence of noise is crucial to basic system design.

If transmit power is determined, path loss values also aid in determining coverage area. For example, in the aircraft navigation system, the maximum allowable distance between GRS units can be found. In a given environment, understanding coverage areas leads to knowledge of possible network topologies.

Chapter 8

Conclusion

The purpose of this project was to perform propagation and siting investigations for a distributed wireless aircraft navigation system. Hardware appropriate for the necessary measurements was identified and developed. Furthermore, various environments and siting methods were selected to mimic the type of abnormal locations in which the system will be deployed. A framework was developed for the investigation that divided the measurements into large-scale deterministic, small-scale statistical, and large-scale statistical measurements. Empirical data from several environments for both large-scale and small-scale fading was collected. Based on these measurements, simple propagation models were formed and results were analyzed. Additionally, communication system design implications were briefly mentioned to act as a bridge between the reported results of this project and the design of the navigation system and other distributed communication systems.

The results of this project pertain directly to wireless system design and performance prediction for both Draper wireless control networks and fourth generation wideband multihop wide area networks. At the physical layer, understanding propagation effects in various environments and site-dependent signal variations leads to knowledge of transmission capability. Incorrect estimates of propagation can lead to complete system and information transfer failure. At the link level, understanding small-scale transmission variation caused by signal loss or fading facilitates link-level design, such as modulation or coding schemes. Since the physical and link-level layers are the bases for network performance and functionality, this project is important to the wireless distributed systems in question. Furthermore, this project reports propagation results from irregular siting that previous work has rarely studied.

While the empirical results from this project cover a wide range of environments and siting methods, additional work in this area can still be performed. The hardware used in all experiments transmitted a narrowband signal. Programming the hardware to output a wideband signal—a feature of which it is capable—would allow measurements of two additional small-scale channel parameters: coherence bandwidth and rms delay spread. Furthermore, estimates of channel impulse responses could be formed. These measurements could yield information leading to additional system performance improvement.

The next milestone for this project involves using the recorded in computer performance simulations of the navigation system. Furthermore, additional hardware units must be built and programmed to act as an entire data communications network. This wireless network, consisting of many individual wireless hosts, will act as a real-life

hardware model of the navigation system. The network can then be deployed into various environments and its link-level performance can be evaluated, moving one step beyond the computer performance simulations that already exist.

This page intentionally left blank

Appendix A

Additional Measurements

Throughout the course of this project, additional measurements were made that do not fit into the general scheme of what was reported, yet are of interest nonetheless. These measurements were done more to investigate the effects of various siting configurations than for propagation modeling purposes.

One issue of interest was to investigate the loss differences between various sitings of the transmitter atop a building. The transmitter was set in various places atop the same parking garage from section 7.2. Figure A-1 is a diagram of the 6 locations where the transmitter was tested. These include right near the edge of the building, as well as on the deck of the building a few feet inwards from the edge. The receiver was set 25 meters away from the building one meter from the ground.

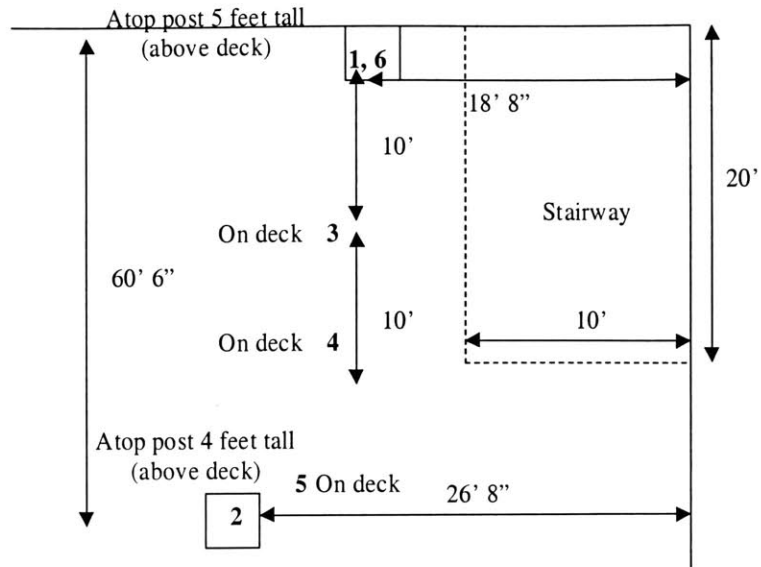


Figure A-1: Transmitter siting locations atop parking garage.

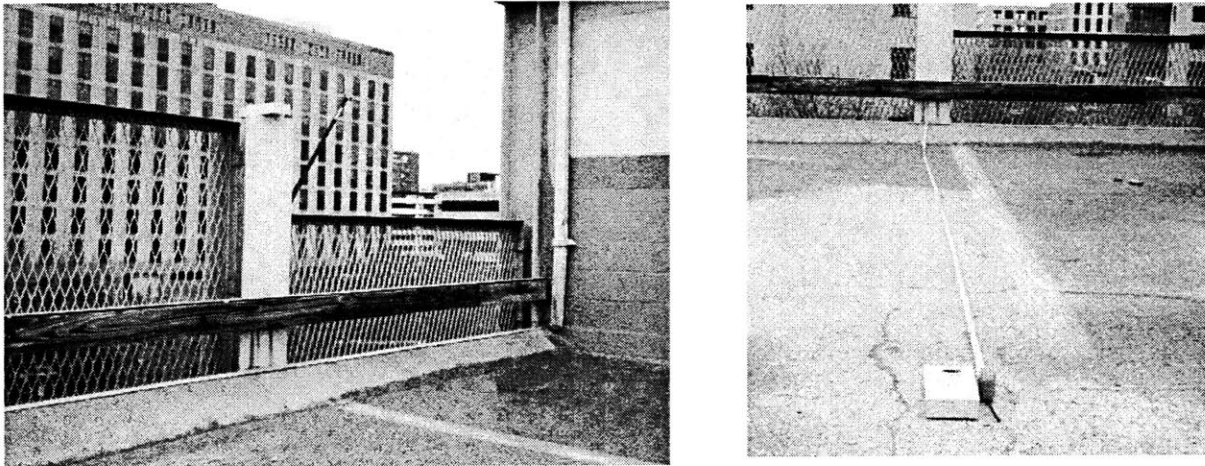


Figure A-2: (a) Transmitter atop post at locations 1 and 6 in Figure A-1. (b) Transmitter on deck of roof at location 3 in Figure A-1.

Depending on the transmitter siting, loss ranged across 15 dB. Siting the transmitter on the edge of the building at points 1 and 6 from Figure A-1 showed the best propagation performance, while the worst performance was seen when the transmitter was on the floor of the deck 60 feet inward from the building edge at point 5.

Another measurement of interest was to observe the difference in path loss between a LOS and an OLOS path around a corner. Two brief experiments were performed for this investigation. The transmitter and receiver were first oriented with a LOS path at Tx1 and Rx1 in Figure A-2. The receiver was then moved to Rx2 around the corner and out of the LOS path. The path loss difference between these two measurements was found to be approximately 20 dB. The receiver was then left at Rx2 and measurements were performed with the transmitter at LOS location Tx2 and OLOS location Tx3. The path loss difference between these two measurements was approximately 10 dB. From these experiments, the large path loss drop-off of RF waves around a corner can be seen.

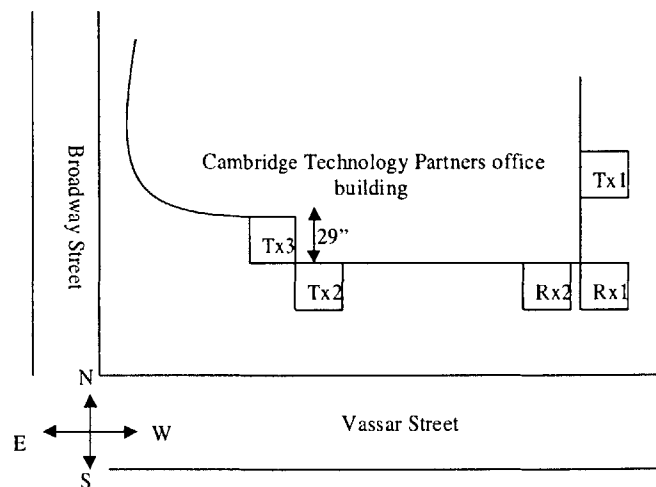


Figure A-3: Diagram of corner measurements.

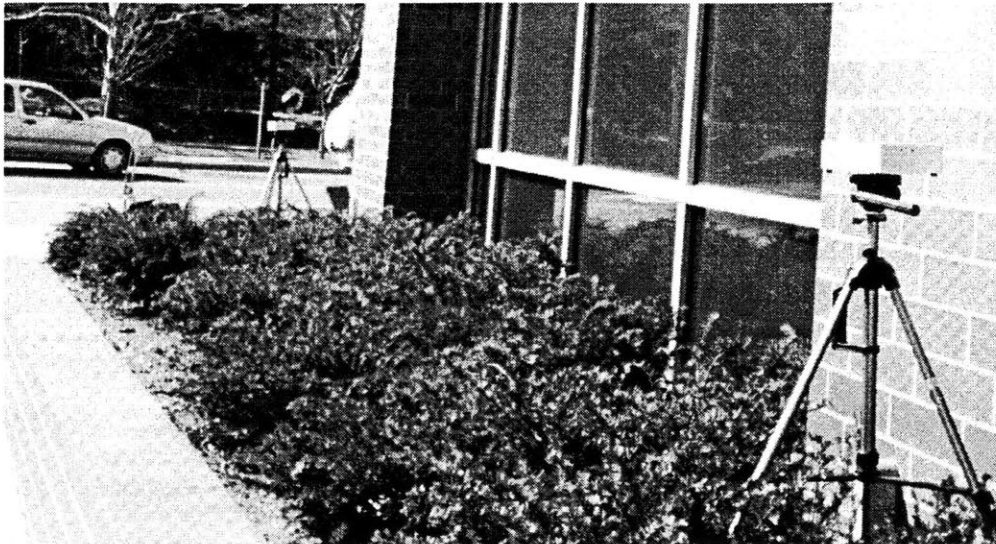


Figure A-4: Photograph of corner measurements with transmitter and receiver in locations Tx1 and Rx1 from Figure A-3.

One final additional measurement performed for this project was a large-scale indoor measurement to investigate propagation through a tunnel. This experiment was performed along the MIT underground hallway under building M56. As seen in Chapter 7, the path loss exponent n was found to be 2.74. It should be noted that this number is smaller than the measured loss exponent for most of the outdoor environments from Chapter 7.

Table A-1 is a table showing the parameters of the theoretical distribution functions as shown in Figure 6-2. The data includes two measurements from the two tree experiments whose histograms are not shown in Chapter 6.

LOCATION	ENVIRONMENT	RAYLEIGH σ	RICEAN K FACTOR	LOGNORMAL μ, σ
Alewife Preserve	Ground-to-ground through vegetation	6.75×10^{-5}	5.37	-9.57, 0.47
Vassar St.	Ground-to-ground urban	1.85×10^{-4}	2.04	-8.49, 0.52
Thorndike Park	Maple tree, no foliage	1.80×10^{-4}	4.21	-8.44, 0.24
Vassar St.	Evergreen tree, foliage	3.01×10^{-4}	-4.47	-7.98, -.55

Table A-1: Theoretical distribution parameters for measurements from section 6.1.

Appendix B

Maps and Photographs

B.1 Alewife Preserve

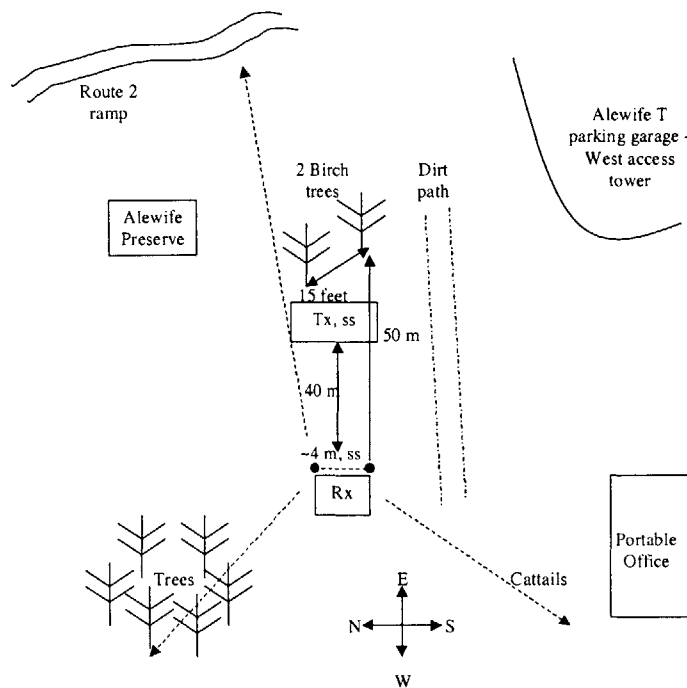


Figure B-1: Diagram of Alewife Preserve measurements. Dotted lines show directions in which large-scale measurements were performed. Small-scale measurement location is shown near the center of the diagram with the 4 m horizontal dimension labeled with "ss." The transmitter, as seen in the diagram, was 40 meters away from the receiver for the small-scale measurements.



Figure B-2: DWN transmitter 1 meter high above low-lying vegetation.



Figure B-3: DWN transmitter amongst low-lying vegetation.

B.2 Vassar Street/Urban Setting

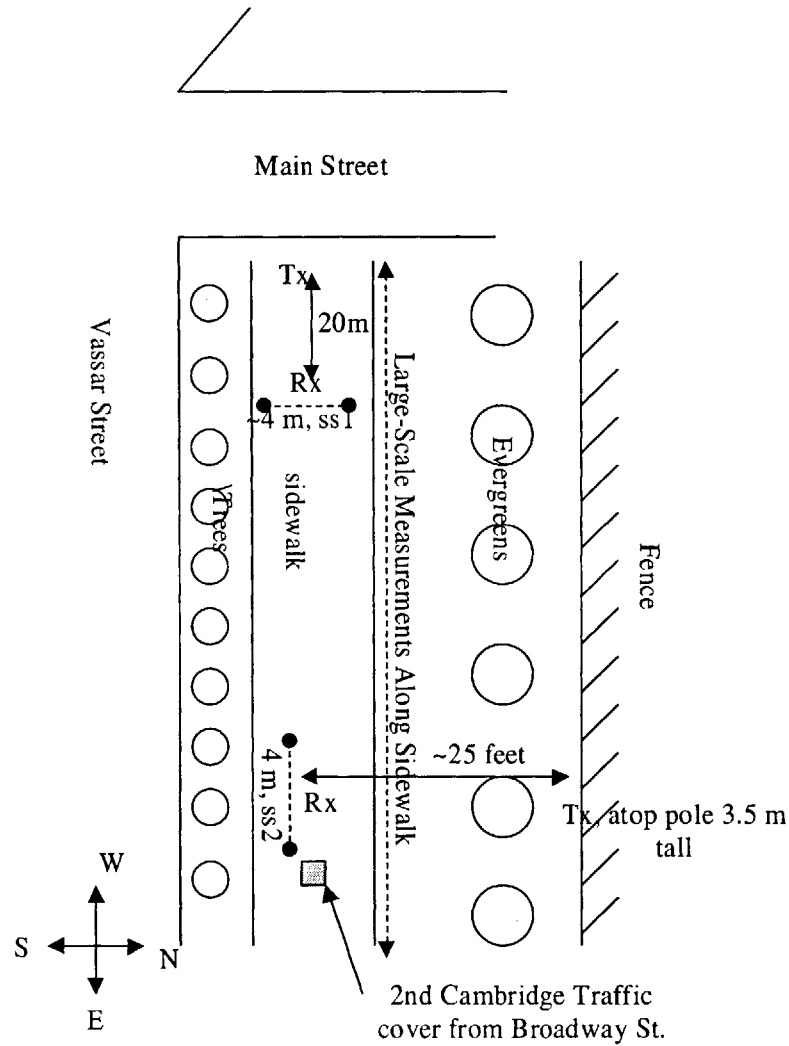


Figure B-4: Diagram of measurements conducted along Vassar Street. Direction of large-scale measurements shown with vertical dotted line. Two small-scale measurement locations are shown: ss1 refers to the small-scale urban measurement and ss2 shows the small-scale measurement conducted through the Evergreen tree. The small-scale Evergreen tree measurements were conducted when no local traffic was present.

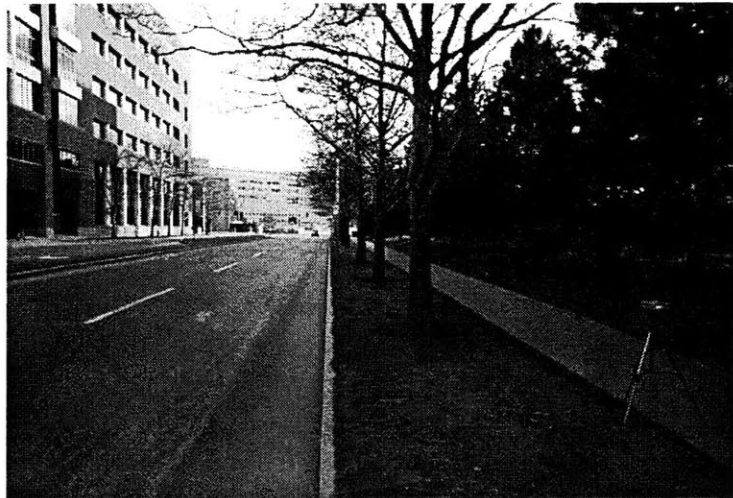


Figure B-5: Picture of Vassar Street along which urban propagation measurements were performed. Cars were present during all measurements, though are not shown above.



B-6: Map of Vassar Street along which large-scale ground-to-ground urban measurements were taken. Measurements were performed along solid white line in map above.

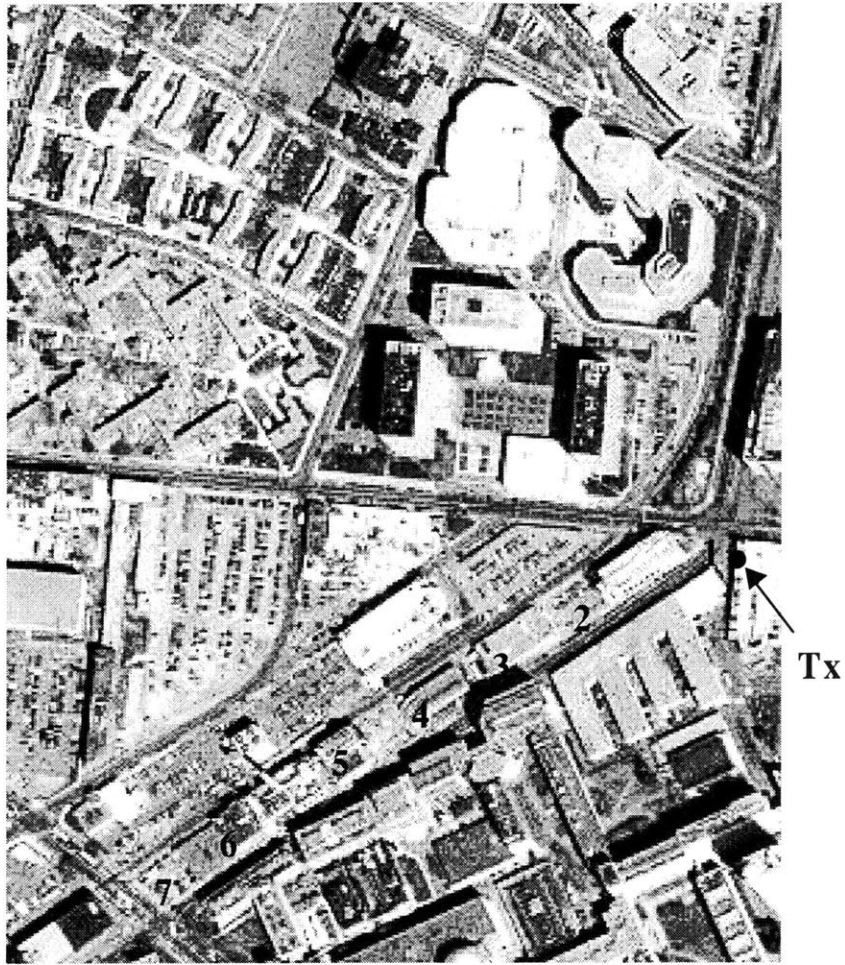


Figure B-7: Map of Vassar Street, along which large-scale measurements were taken with transmitter at the top of a parking garage. Numbers in map show locations of where measurements were performed.

B.3 Thorndike Park

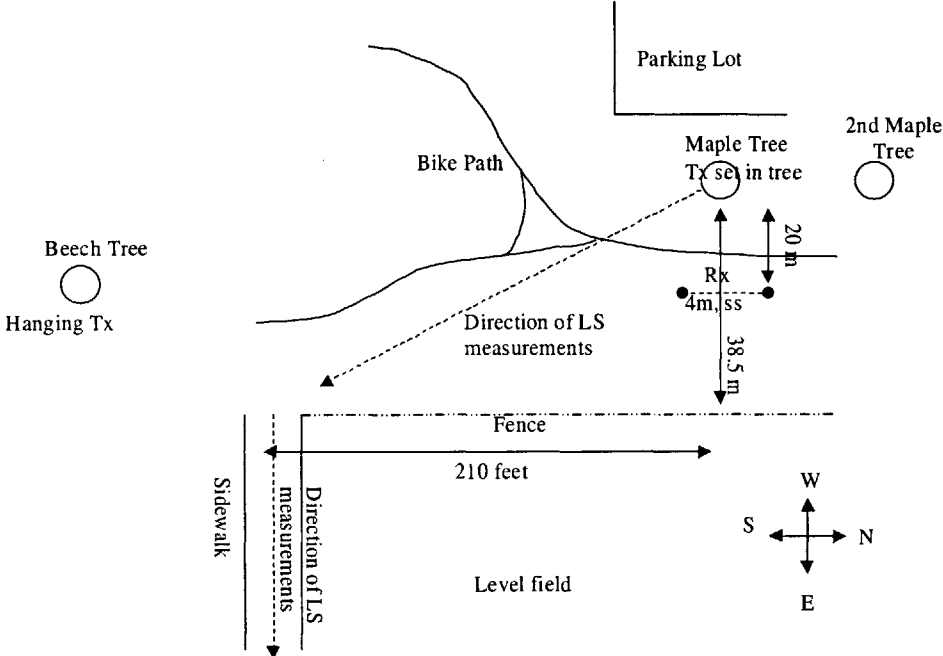


Figure B-8: Diagram of Thorndike Park measurements—area where most tree measurements were performed. The maple tree is in the upper right corner of the map and the direction of the large-scale measurements is shown with dotted lines. The small-scale measurement is denoted with ‘ss’ in the map. The Beech tree from which the transmitter was hung for small-scale coherence time measurements is found on the left side of the map.



Figure B-9: Photograph of transmitter atop pole set in Maple tree with no foliage.

Appendix C

Hardware Overview Chart

Tables C-1 and C-2 list various hardware options reviewed before the DWN transceiver was selected as the hardware for the propagation measurement equipment.

MANUFACTURER	HARDWARE	WAVEFORMS	RANGE	DATA RATE
Intersil	Prism II chipset	802.11 Direct Sequence Spread Spectrum	1000 ft	11 Mbps
Ericsson	Bluetooth Development Kit	Bluetooth Fast Frequency Hopping (1600 hops/second)	1-10 m	1 Mbps
National Semiconductor	LMX3162 Evaluation Board	Bluetooth	1-10 m	1 Mbps
Philsar	Bluetooth Evaluation Board	Bluetooth	1-10 m	1 Mbps
American Microsystems	DEV6143	Narrowband or spread spectrum, adjustable chip-rate and modulation schemes	?	4 Mbps
Draper	DWN transceivers	Binary FSK or CW	> 150 m	57.6 kbps
Berkeley Varitronics	Duet Channel Sounder	IS-95 CDMA		
Linx Technologies	LINX transmitter	FSK		

Table C-1: Hardware overview.

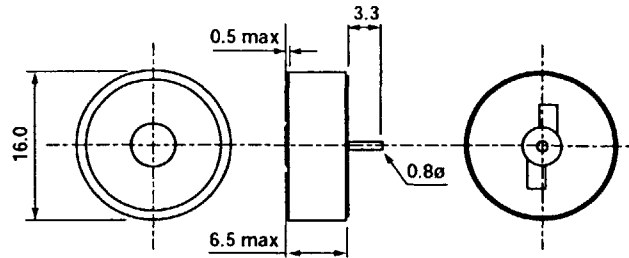
MANUFACTURER	HARDWARE	FREQUENCY	COMMENTS
Intersil	Prism II chipset	2.4 GHz	Difficult to alter hardware and software for measurements
Ericsson	Bluetooth Development Kit	2.4 GHz	Bluetooth not proven standard
National Semiconductor	LMX3162 Evaluation Board	2.4 GHz	Empty board, must obtain components separately (time)
Philsar	Bluetooth Evaluation Board	2.4 GHz	Was not released at the time of research
American Microsystems	DEV6143	Adjustable	Difficult to change hardware for measurements
Draper	DWN transceivers	2.4 GHz	Programmable, upgradeable
Berkeley Varitronics	Duet Channel Sounder	PCS 1930-1990 MHz Cellular 868-896 MHz ISM 2.4-2.485 GHz	Not upgradeable to link level communication
Linx Technologies	LINX transmitter	900 MHz	Not upgradeable to link level communication

Table C-2: Hardware overview.

Appendix D

Antenna Data Sheets

DAC Series



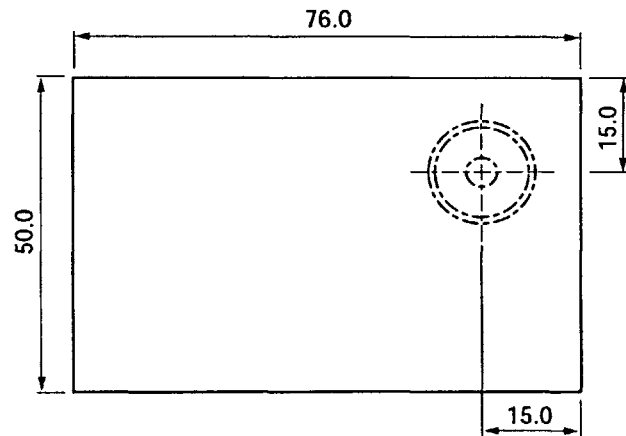
Unit: mm

Features

- Vertical Polarization reception
- Low profile (6.5mm max)
- Omni-directional in azimuth
- Low interference design
- Central feeding point terminal
- Wide bandwidth
- Light weight

Description

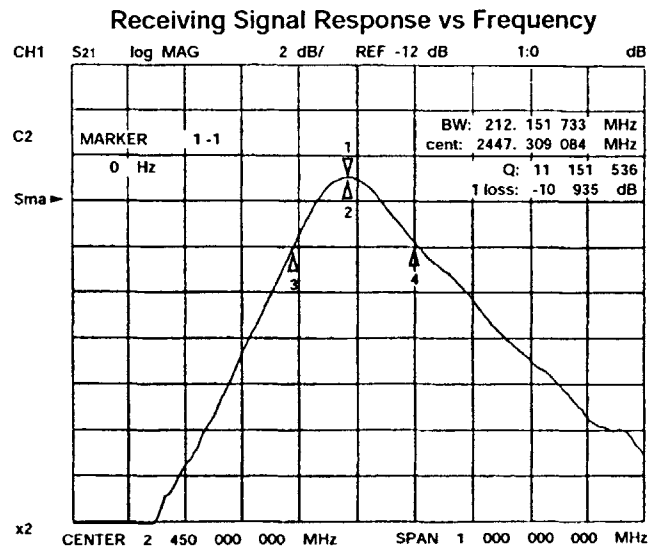
The DAC Series is a miniature dielectric antenna element for 2.4 GHz wireless LAN systems. This antenna has vertical polarization characteristics. TOKO's proprietary ceramic dielectric material provides excellent stability and sensitivity. It is mountable in Type II extended PCMCIA cards.

Mounted with ground Plane

Unit: mm

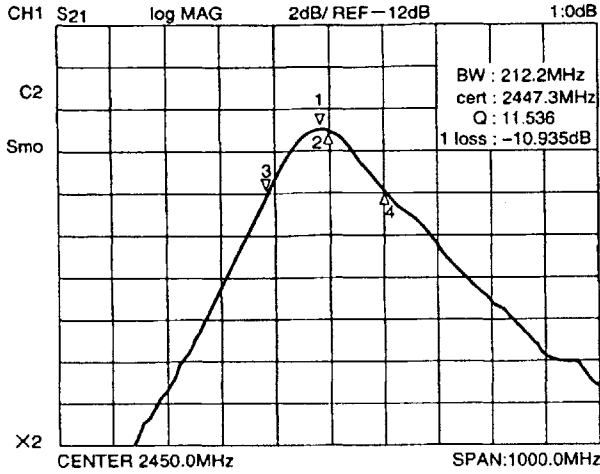
SPECIFICATIONS

Part Number	DAC2450CT1T
Center Frequency	2450 MHz
3dB Receiving Bandwidth	±50 MHz min.
Impedance	50Ω
Peak Gain (Azimuth)	-4 dBi typ.
Peak Gain (Elevation)	0 dBi typ.
Operating Temperature	-10 ~ +60° C
Storage Temperature	-20 ~ +85° C
Weight	4.3g

TYPICAL CHARACTERISTICS

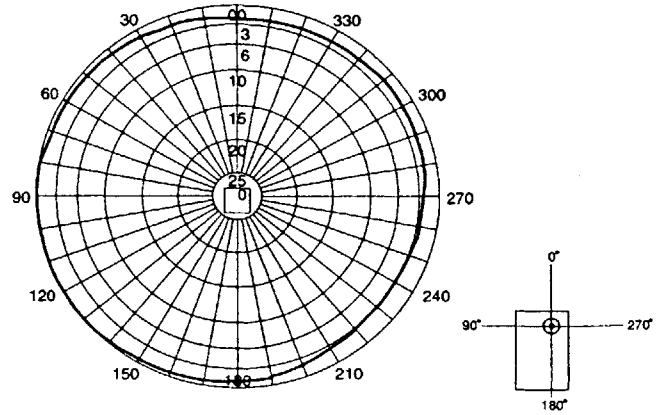
ELECTRICAL CHARACTERISTICS

Receiving Signal Responce vs Frequency

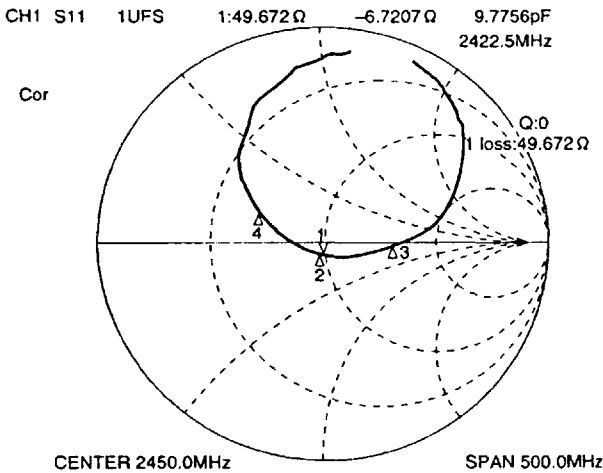


DIELECTIVITY CHARTS

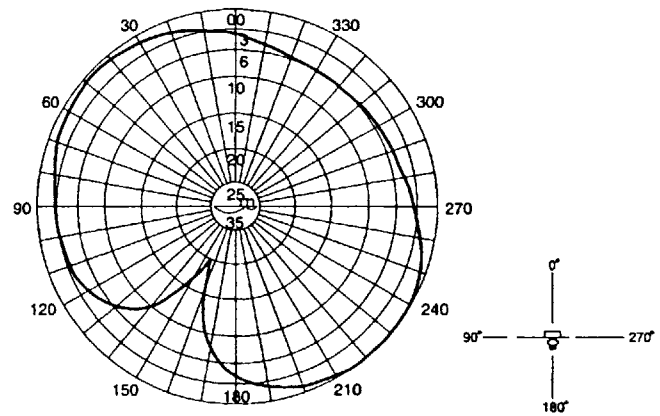
Horizontal Pattern



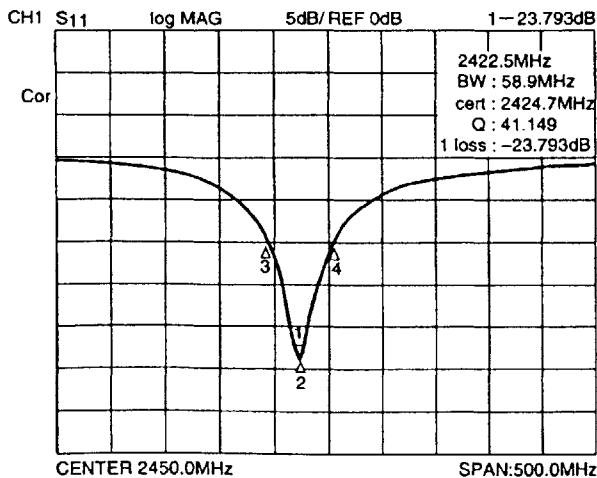
Smith Impedance



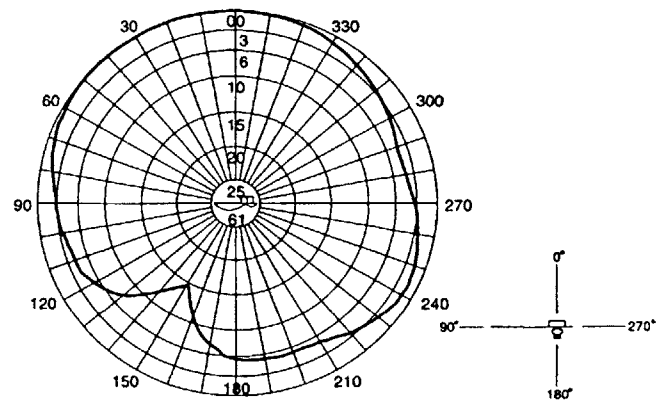
Vertical Pattern



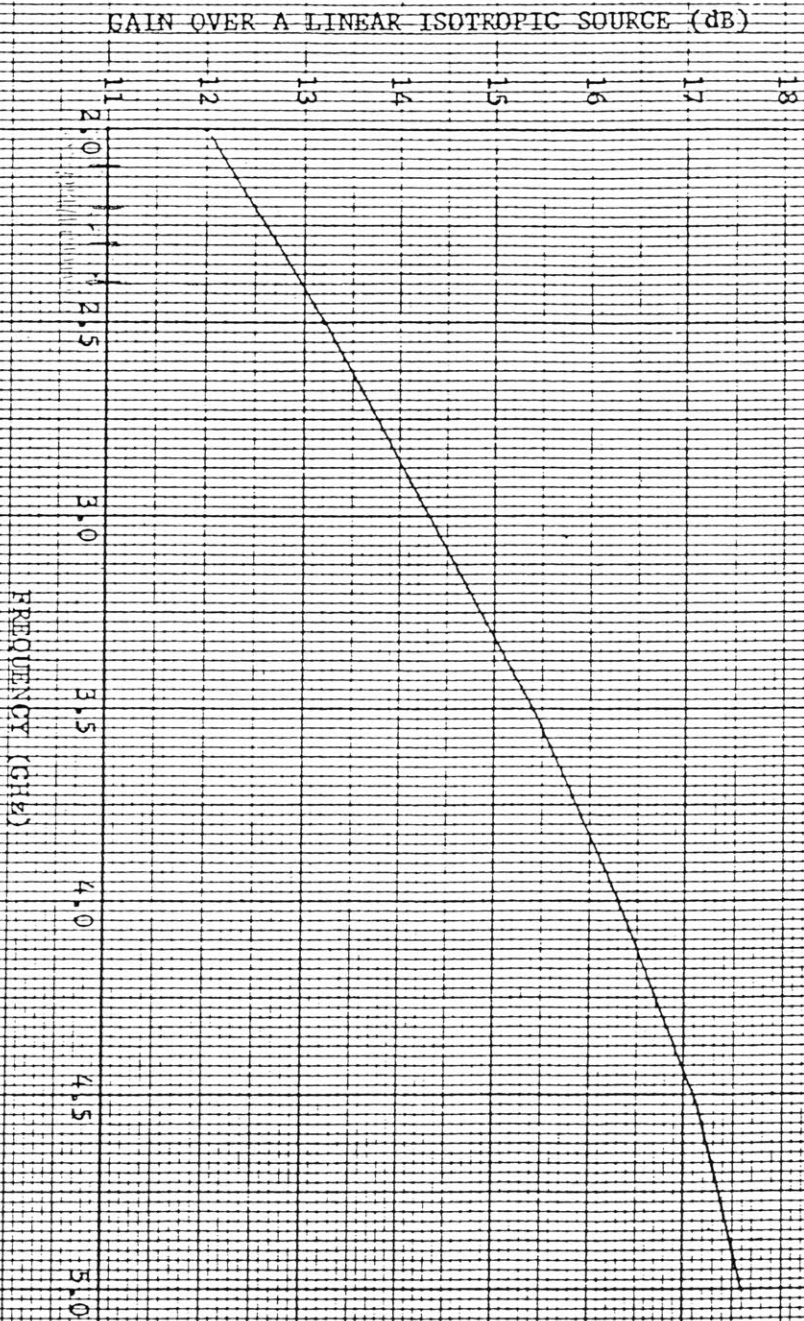
Return Loss



Vertical Pattern



AEL Datasheet



HORN ANTENNA
AEL MODEL H-510E
TYPICAL GAIN VS. FREQUENCY

EMCO Datasheet

Typical Antenna Calibration and Power Requirements at
1 Meter Spacing 300 Watts Maximum Continuous Power

FREQUENCY (MHz)	ANTENNA FACTOR (db)	GAIN (dB)	GAIN NUMERIC	FIELD STRENGTHS (E)				
				1 V/M	10 V/M	20 V/M	100 V/M	200 V/M
1000	24.4	5.8	3.77	0.01	0.9	3.5	88.3	*
1500	25.7	8.1	6.40	0.01	0.5	2.1	52.0	208.2
2000	28.4	7.9	6.14	0.01	0.5	2.2	54.3	217.2
2500	29.4	8.7	7.49	0.00	0.4	1.8	44.5	178.1
3000	31.0	8.8	7.56	0.00	0.4	1.8	44.1	176.4
3500	32.2	8.9	7.78	0.00	0.4	1.7	42.9	171.4
4000	33.8	8.5	7.08	0.00	0.5	1.9	47.1	188.3
4500	33.0	10.2	10.57	0.00	0.3	1.3	31.5	126.1
5000	34.7	9.5	8.99	0.00	0.4	1.5	37.1	148.3
5500	35.4	9.6	9.16	0.00	0.4	1.5	36.4	145.6
6000	35.4	10.4	10.98	0.00	0.3	1.2	30.4	121.4
6500	35.7	10.8	11.91	0.00	0.3	1.1	28.0	111.9
7000	36.5	10.6	11.58	0.00	0.3	1.2	28.8	115.1
7500	37.8	9.9	9.80	0.00	0.3	1.4	34.0	136.1
8000	38.0	10.2	10.58	0.00	0.3	1.3	31.5	126.0
8500	38.1	10.7	11.62	0.00	0.3	1.1	28.7	114.8
9000	38.4	10.9	12.34	0.00	0.3	1.1	27.0	108.1
9500	38.4	11.4	13.85	0.00	0.2	1.0	24.1	96.3
10000	38.5	11.7	14.83	0.00	0.2	0.9	22.5	89.9
10500	38.6	12.0	16.00	0.00	0.2	0.8	20.8	83.3
11000	39.0	12.1	16.17	0.00	0.2	0.8	20.6	82.4
11500	39.3	12.2	16.50	0.00	0.2	0.8	20.2	80.8
12000	39.4	12.4	17.55	0.00	0.2	0.8	19.0	76.0
12500	39.0	13.2	20.76	0.00	0.2	0.6	16.1	64.2
13000	39.9	12.6	18.05	0.00	0.2	0.7	18.5	73.9
13500	41.3	11.6	14.34	0.00	0.2	0.9	23.2	93.0
14000	41.4	11.7	14.76	0.00	0.2	0.9	22.6	90.3
14500	41.3	12.1	16.20	0.00	0.2	0.8	20.6	82.3
15000	39.9	13.8	23.98	0.00	0.1	0.6	13.9	55.6
15500	37.9	16.1	40.66	0.00	0.1	0.3	8.2	32.8
16000	38.2	16.1	40.43	0.00	0.1	0.3	8.2	33.0
16500	39.8	14.7	29.82	0.00	0.1	0.4	11.2	44.7
17000	41.7	13.2	20.66	0.00	0.2	0.6	16.1	64.5
17500	44.6	10.4	11.08	0.00	0.3	1.2	30.1	120.3
18000	46.9	8.4	6.96	0.00	0.5	1.9	47.9	191.7

This page intentionally left blank

Bibliography

- [1] T. S. Rappaport and C. D. McGillem, "UHF fading in factories," *IEEE Journal on Selected Areas in Communication*, Vol. 7, No. 2, 1989, pp.40-48.
- [2] K. Pahlavan and S. J. Howard, "Doppler spread measurements of indoor radio channel," *Electronics Letters*, Vol. 26, No. 2, 1990, pp. 107-108.
- [3] H. Hashemi, "Impulse response modeling of indoor radio propagation channels," *IEEE Journal on Selected Areas in Communication*, Vol. 11, No. 7, 1993, pp. 967-978.
- [4] H. Hashemi, "The indoor propagation channel," *Proceedings of the IEEE*, Vol. 81, No. 7, 1993, pp. 943-968.
- [5] J. Van Rees, "Measurements of the wide-band radio channel characteristics for rural, residential, and suburban areas," *IEEE Transactions on Vehicular Technology*, Vol. 36, No. 1, 1987, pp. 2-6.
- [6] R. H. Raekken, H. Langass, G. Lovnes, and S. E. Paulse, "Wideband impulse response measurements at 900 MHz and 1.7 GHz," *GLOBECOM '91 Global Telecommunications Conference*, Vol. 2, 1999, pp. 1303-1307.
- [7] G. M. Chiasson, J. F. Kepler, P. D. Rasky, and D. M. Tolli, "Field measurements of a prototype slow frequency hop personal communication system," *IEEE Vehicular Technology Conference*, Vol. 1, 1995, pp. 118-124.
- [8] D. J. Purle, S. C. Swales, and M. A. Beach, "Propagation characteristics of a frequency hopped channel," *Ninth International Conference on Antennas and Propagation*, Vol. 2, 1993, pp. 861-864.

- [9] V. Erceg, S. S. Ghassemzadeh, M. Taylor, D. Li, and D. L. Schilling, "Urban/suburban out-of-sight propagation modeling," *IEEE Communications Magazine*, Vol. 30, No. 6, 1992, pp. 56-61.
- [10] S. Mockford, A. M. D. Turkmani, and J. D. Parsons, "Local mean signal variability in rural areas at 900 MHz," *40th IEEE Vehicular Technology Conference*, 1990, pp. 610-615.
- [11] T. S. Rappaport, *Wireless Communications: Principles and Practice*, Upper Saddle River, NJ: Prentice Hall, 1996.
- [12] V. K. Garg, *IS-95 CDMA and CDMA 2000, Cellular/ PCS Systems Implementation*, Ch. 12, Upper Saddle River, NJ: Prentice Hall, 2000.
- [13] M. Hata, "Empirical formula for propagation loss in land mobile radio services," *IEEE Transactions on Vehicular Technology*, Vol. 29, No. 3, 1980, pp. 317-325.
- [14] N. Patwari, G. D. Durgin, T. S. Rappaport, R. J. Boyle, "Peer-to-peer low antenna outdoor radio wave propagation at 1.8 GHz," *49th IEEE Vehicular Technology Conference*, Vol. 1, 1999, pp. 371-375.
- [15] R. A. Foran, T. B. Welch, and M. J Walker, "Very near ground radio frequency propagation measurements and analysis for military applications," *Military Communications Conference Proceedings*, Milcom 1999, Vol. 1, 1999, pp. 336-340.
- [16] K. Pahlavan and A. H. Levesque, *Wireless Information Networks*, Ch. 3-4, New York: John Wiley and Sons, 1995.
- [17] B. Sklar, "Rayleigh fading channels in mobile digital communication systems, Part I: characterization," *IEEE Communications Magazine*, Vol. 35, No. 9, 1997, pp. 136-146.
- [18] J. B. Andersen, T. S. Rappaport, S. Yoshida, "Propagation measurements and models for wireless communication channels," *IEEE Communications Magazine*, Vol. 33, No. 1, 1995, pp. 42-49.
- [19] M. Dolukhanov, *Propagation of Radio Waves*, Moscow: Mir Publishers, 1971.
- [20] G. P. Ohman, "Universal curves for the horizontal polarization reflection coefficient," *IRE Transactions on Antennas and Propagation*, Vol. 10, 1962, pp. 450-452.

- [21] G. P. Ohman, "Universal curves for the vertical polarization reflection coefficient," *IRE Transactions on Antennas and Propagation*, Vol. 5, 1957, pp. 140-142.
- [22] R. H. Clarke, "A statistical theory of mobile radio reception," *Bell Systems Technology Journal*, Vol. 47, 1968, pp. 957-100.
- [23] H. Suzuki, "A statistical model for urban radio propagation," *IEEE Transactions on Communications*, Vol. 25, No. 7, 1977, pp. 673-680.
- [24] P. A. Bello, "Characterization of randomly time-variant linear channels," *IEEE Transactions on Communication Systems*, Vol. 11, 1963, pp. 360-393.
- [25] S. Stein, "Fading channel issues in system engineering," *IEEE Journal on Selected Areas in Communications*, Vol. 5, No. 2, 1987, pp. 68-89.
- [26] B. Sklar, "Rayleigh fading channels in mobile digital communication systems, Part II: mitigation," *IEEE Communications Magazine*, Vol. 35, No. 9, 1997, pp. 148-155.
- [27] B. Sklar, *Digital Communications: Fundamentals and Applications*, Upper Saddle River, NJ: Prentice Hall, 1988.
- [28] J. G. Proakis and M. Salehi, *Communication Systems Engineering*, Upper Saddle River, NJ: Prentice Hall, 1994.